Assessing the Impacts of Greenhouse Gasses on Upwelling and Surface Temperature in the
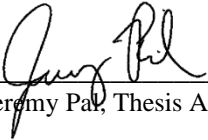California Current System

By Kevin McGee

A Thesis Paper Presented to the

Faculty of the Department of
Civil Engineering and Environmental Science
Loyola Marymount University

In Partial fulfillment of the Requirements for the Degree
Master of Science in Engineering in Civil Engineering
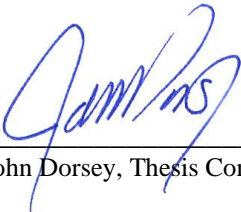

March 8, 2020

I am submitting herewith a thesis written by Kevin McGee entitled "Assessing the Impacts of Greenhouse Gasses on Upwelling and Surface Temperature in the California Current System." I have examined the final electronic copy of this thesis for form and content and recommend that it be accepted in partial fulfillment of the requirements for the degree of Master of Science in Engineering in Civil Engineering.

_____

Jeremy Pal, Thesis Advisor

We have reviewed the thesis and recommend its acceptance:
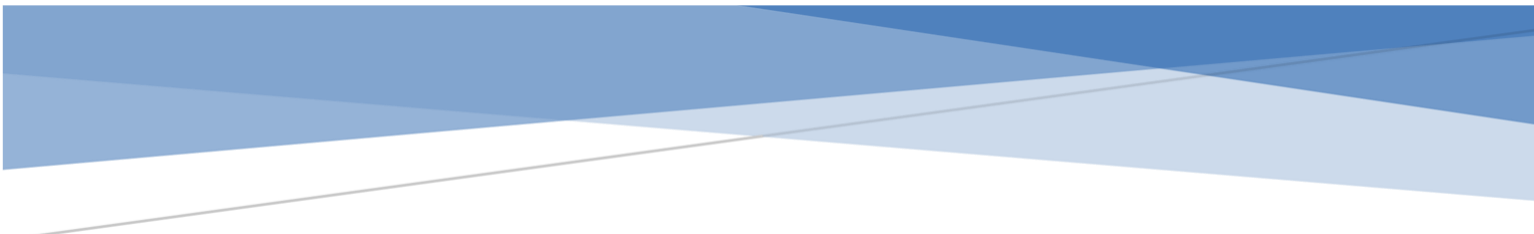
_____

John Dorsey, Thesis Committee Member

_____

Donald R. Kendall, Thesis Committee Member

_____

Pengfei Xue, Thesis Committee Member

Assessing the Impacts of Greenhouse Gasses on Upwelling and Surface Temperature in the California Current System

By Kevin McGee

A Thesis Paper Presented to the
Faculty of the Department of
Civil Engineering and Environmental Science
Loyola Marymount University

In Partial fulfillment of the Requirements for the Degree
Master of Science in Engineering in Civil Engineering

Contents

Acknowledgements

This study would not have been possible without the guidance of Dr. Jeremy Pal. I will always be grateful for his willingness to take the time to help with this project at any time he was available. I would like to thank the members of my committee including Dr. Donald Kendall, Dr. Pengfei Xue, and Dr. John Dorsey. I extend my gratitude to Oak Ridge National Laboratory for allowing us to utilize their latest climate projections and to Dr. Moetasim Ashfaq for all the correspondence over the past 2 years. Lastly, a big thank you to my family – especially to my parents and Stephanie Horwitz – for the continued support and encouragement.

Abstract

The California Current system (CCS) is home to a vast and diverse marine coastal ecosystem. Upwelling is an oceanic phenomenon wind-driven displacement of surface water brings cold nutrient-rich water from the ocean bottom to surface waters. Along the coast in the CCS, upwelling occurs via the advection of water perpendicular to the shoreline northerly winds, a phenomenon called "Ekman Transport". In the open ocean. Wind stress curl causes disruption of normal currents, resulting in small pockets of upwelled or downwelled water (downwelling is the movement of water downward in the ocean, the opposite of upwelling). This process is called "Ekman Pumping", and over large swaths of ocean, it can result in a notable increase/decrease in net upwelling. Upwelling is one of the main driving forces behind the diversity and strength of the ecosystems within the CCS.

The Bakun hypothesis (Bakun, 1990) suggests that with the future increase of atmospheric greenhouse gases (GHGs), Eastern Boundary Upwelling Systems (EBUSs) will experience an increase in upwelling intensity and season duration. The Bakun hypothesis has been proven to be an accurate description of the mechanisms of change expected in all major EBUSs in the world, except for the CCS, where only weak correlations have been made (Sydeman, García-Reyes, Schoeman, D. S. Rykaczewski, R. R. . Thompson, Black, & Bograd, 2014). A recent study by Wang et al. 2015 found weak correlations of decreases in upwelling intensity in the CCS, which would suggest that the Bakun Hypothesis does not accurately depict the future of the CCS. Previous climate change CCS studies have relied on atmosphere-ocean global climate models (AOGCMs), which are typically performed on a horizontal grid too coarse to accurately depict the physical changes expected in the CCS.

In this study, a 10-member ensemble of high resolution regional climate model (RCM) climate change experiments driven by 10 AOGCMs is used to project changes in the timing and intensity of the upwelling season within the CCS and test the Bakun Hypothesis. We also consider Surface Temperature to extrapolate how changes, if any, compound or counteract the accuracy of the Bakun Hypothesis. We find a significant decrease of $6 \text{ m}^3/\text{s}/100\text{m}$ in mean Ekman Transport and an increase of 1.3 ⁰C in mean Surface Temperature. A 1.1×10^{-06} m/s decrease in mean Ekman Pumping is also observed, but these findings are not robust. We also find no change to the length or timing of the upwelling season. The decrease in Ekman Transport and increase in Surface Temperature could compound upon each other and cause damage to vulnerable ecosystems within the CCS, most notably in the latitudinal range of 34°-40° along the coast, as future GHGs concentrate in the atmosphere. In the shallow ocean, decreased upwelling intensity and increased stratification will inhibit the movement of nutrients that primary producers rely on, thus stifling phytoplankton and zooplankton growth. Increases in surface temperature could also create new avenues of environmental stress that local communities are not prepared to adapt to, resulting in decreased physiological performance and potentially geographical shifts in species residence. These changes to shallow ocean communities could have cascading effects on the availability of prey up the trophic web. In the deeper ocean, decreased upwelling intensity and increased stratification will inhibit ocean mixing, and thus decrease availability of dissolved oxygen in the deeper ocean. This could result in hypoxic and anoxic events and create major species die-off in local communities.

Tables and Figures

Figures

Tables

1 Introduction

The California Current System (CCS) is home to a very rich and abundant coastal ecosystem. The CCS is classified as an Eastern Boundary Upwelling System (EBUS). EBUS are current systems along the eastern boundary of an ocean that experience upwelling via surface winds and Ekman transport. Upwelling within EBUSs draws ample nutrients from depth to surface water, allowing for a rich phytoplankton population. This population serves as the base for a trophic pyramid that sustains a myriad of fish, seabirds and marine mammals (Bakun, 1990). In California, upwelling almost exclusively occurs between April – September.

As atmospheric greenhouse gases (GHGs) are expected to rise due to anthropogenic emissions, surface temperature is expected to increase. With rising temperatures, pressure gradients between the land and ocean will increase. This gradient determines the strength of upwelling-favorable winds, the main driver of an upwelling event. Therefore, as GHGs are expected to increase, the upwelling intensity and season length is also expected to increase. This is called the "Bakun Hypothesis" due to a paper by Bakun 1990 where this phenomenon was first described. Although the intensification of upwelling may initially increase the availability of food in the trophic web, it can be intensified to the point where an event will have major adverse effects to the population (Bakun, 1990; Cury & Roy, 1989; Ruzicka, Brink, Gifford, & Bahr, 2016).

Rising temperatures may also cause negative impacts to coastal environments outside the realm of upwelling. Increased temperatures may directly affect populations by creating heat stress outside the tolerance capabilities of a species, potentially causing physiological performance issues, influencing the specific breeding temperature ranges of many fish and

dictating locations viable for a species. Indirectly, increased temperature may cause increased vertical stratification in the ocean, which could lead to decreased nutrient mixing, hypoxia and dead zone events on the continental shelf (Grantham, Brian A., Chan, Francis, & Barth3, 2004; Kirincich et al., 2008).

Previous studies have projected the role GHGs may play in increased upwelling intensities and temperature rise in the CCS (e.g., Snyder et al. 2003; Sydeman et al. 2014; Wang et al. 2015). Snyder et al. 2003 used 40km resolution models to test the Bakun Hypothesis. This study found small increases in upwelling intensity in the CCS, but smaller resolution is required. Wang et al. 2015 used 100km resolution AOGCMs to test the Bakun Hypothesis in the 4 major EBUSs around the world (CCS, Humboldt, Benguela and Canary). They found consistent trends of increasing upwelling in the future at all EBUSs accept for the CCS, where they found weak decreasing trends. Sydeman et al. 2014 was a meta analysis of 22 papers between 1990-2012 on the Bakun Hypothesis in the CCS. As a general trend, found that Bakun's Hypothesis is an accurate mechanism that is occurring in EBUSs.

This study builds on these with models. First, our model's resolution (18 km x 18 km) is much higher than AOGCM models used in past studies (100 km x 100 km or more), providing a more detailed representation of complex coastlines and atmospheric processes. Second, this study's 10-member ensemble will account for intermodal variability, providing more confidence in the study's findings. Therefore, the model used in our study should be able to increase the accuracy and reliability of our results.

The intent of this thesis is to develop high-resolution projections of changes to upwelling intensity by increased atmospheric GHGs in the California Current System by dynamically downscaling an ensemble of global climate models. The enhanced model resolution allows us to

understand the changes in upwelling intensity and the large model ensemble allows us to provide an assessment of projection uncertainty. This study addresses:

- the impact of GHGs on coastal water temperatures
- the impact of GHGs on upwelling intensity
- the impact of GHGs on upwelling season timing and duration
- The interplay of these two impacts on coastal aquatic ecosystems

From our findings, we extrapolate how changes, if any, affect coastal marine ecosystems and the fisheries that rely on them.

1.1 Background

The California Current system (CCS) is a Pacific Ocean current system moving south from Alaska to Baja California. This wind driven surface current allows for the existence of the vast and diverse marine ecosystem present along this coastline. This ecosystem supports over $5.5 billion in landings revenues, a notable section of the world fishery economy (National Marine Fisheries Service, 2014). Preserving the resources of this ecosystem is of vital importance to coastal health and coastal communities.

Upwelling, the driving force behind the diversity and strength of this ecosystem, is a phenomenon that occurs in the CCS with the presence northerly or northwesterly winds. These winds are driven by the Pacific High, the semi-permanent subtropical high-pressure system formed by the descending air at the intersection of the Hadley and Ferrel cells in the Pacific Ocean. As air is brought down from the atmosphere, high pressure surface air begins to move outwards towards low pressure areas surrounding the Pacific High. As the wind begins to move outward, the Coriolis Effect, the inertial force felt by the wind caused by the rotation of the earth, twists the wind vectors clockwise in the Northern Hemisphere (counterclockwise in the Southern Hemisphere). The result is a high-pressure block with constant surface winds moving around it clockwise.

In the boreal summer, when the sun oriented towards the northern hemisphere, the Pacific High migrates northward towards Alaska. Surface winds with geostrophic flow – winds flowing parallel to pressure gradient isobars due to the pressure gradient force balancing the Coriolis force – blow alongshore from the north (referred to as "upwelling-favorable winds" in this study). The surface frictional force resulting from these winds causes surface waters to move to the south. At the same time, the Coriolis force provides water with a clockwise twisting motion, producing a net transport of water west, perpendicular to the coast. This phenomenon, where

water moves 90° clockwise to the direction of the wind affecting it, is called Ekman transport (Figure 1).

In order to balance the loss of surface water caused by Ekman transport, cool, nutrient-rich water is drawn up from depth, and nutrients essential to primary productivity and larval/juvenile fish development permeate into the surface layer (Figure 1). Ekman transport velocity is the most commonly used and simple quantitative measurement of upwelling intensity (Schwing, O'Farrel, Steger, & Baltz, 1996). The phytoplankton growth that results supports the rich trophic food web that exists along the west coast of North America and sustains some of the largest fishing markets around the world (Pauly & Christensen, 1995).
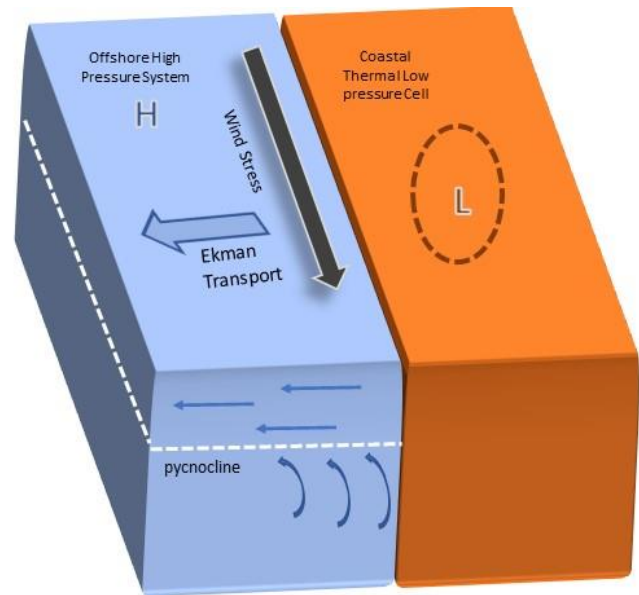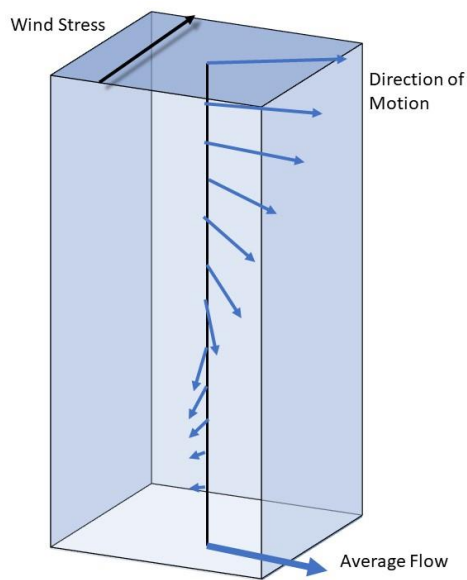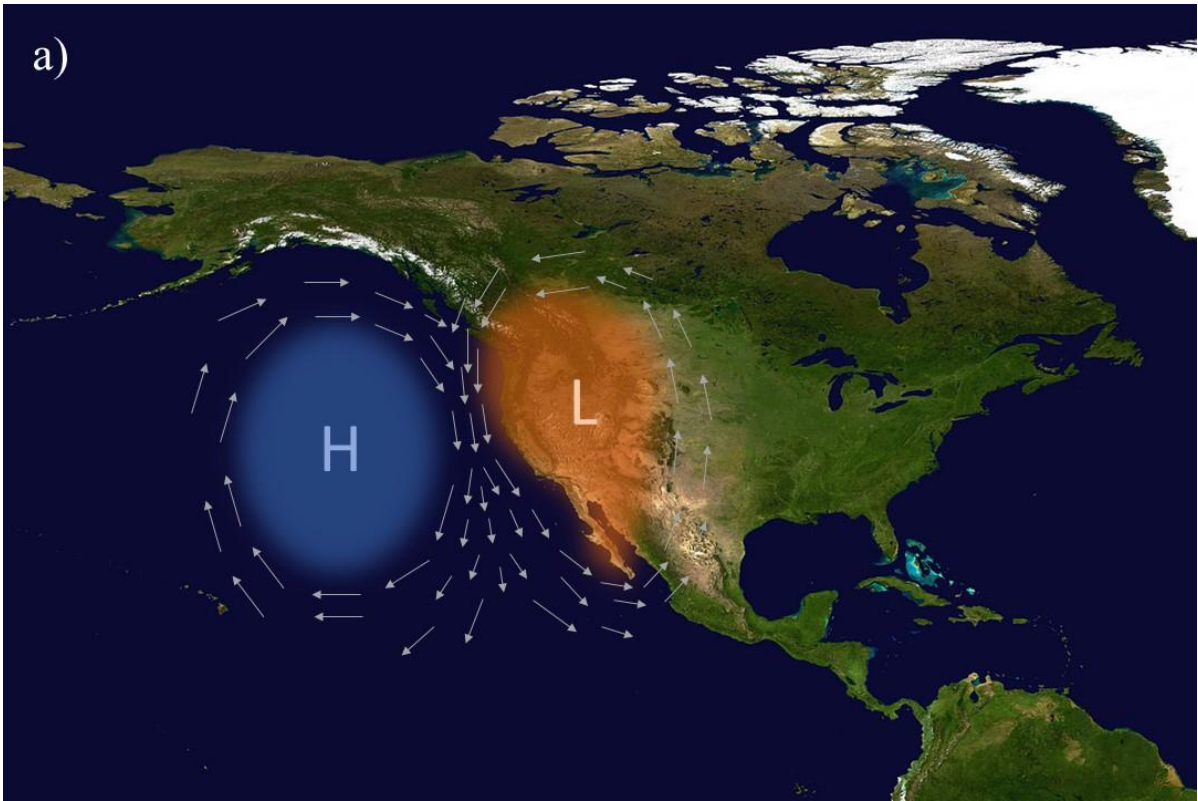
Figure 1: Ekman Transport and Upwelling in the California Current System
a) displays the gradient between the Pacific High offshore pressure system and the thermal low-pressure system of the land. This gradient creates surface winds, which blow along the surface of the coastal ocean in the CCS. In b), the motion created by the wind stress is increasingly twisted by Coriolis force as it descends the water column, creating an "Ekman Spiral", where the net movement of water is perpendicular to the right hand of the surface winds. In c) this perpendicularly displaced surfaced water is replaced by nutrient rich water from the deep ocean. This "upwelled" water promotes water mixing across the ocean pycnocline, which provides surface water with nutrients and replenishes O2 in the deeper ocean.

1.2 The Effect of Climate Change on Upwelling

Bakun 1990 hypothesized that with the future increase of GHGs in our atmosphere, heating on land will intensify during the day more rapidly than over the coastal ocean due to the higher heat capacity of water compared to land. This leads to an increase in the thermal pressure gradient between the high pressure coastal ocean (Pacific high) and lower pressure land. The strengthening of the thermal pressure gradient would work strengthen upwelling-favorable winds, resulting in an increase in local upwelling circulation. This hypothesis as come to be known as the Bakun Hypothesis (Figure 2).

The Bakun Hypothesis has been extensively tested, and has found as a general trend to be an accurate mechanism occurring within most EBUSs. In 2014, Sydeman et al. published a meta-analysis of the available literature on EBUSs and the Bakun Hypothesis. This analysis aggregated and reviewed results from 22 different studies published between 1990 and 2012. The findings of Sydeman et al. support the Bakun Hypothesis, noting that changes in upwelling due to GHG-driven upwelling-favorable winds may be subtle and spatially variable (Sydeman et al., 2014).

By the end of the 21st century, heating over land caused by GHGs is expected to increase as much as 1.4 – 1.7 times more than over the ocean (IPCC, 2014). If the Bakun Hypothesis continues to accurately describe trends in upwelling, the increasing land-ocean pressure gradient may drastically alter the intensity of upwelling events within the CCS.
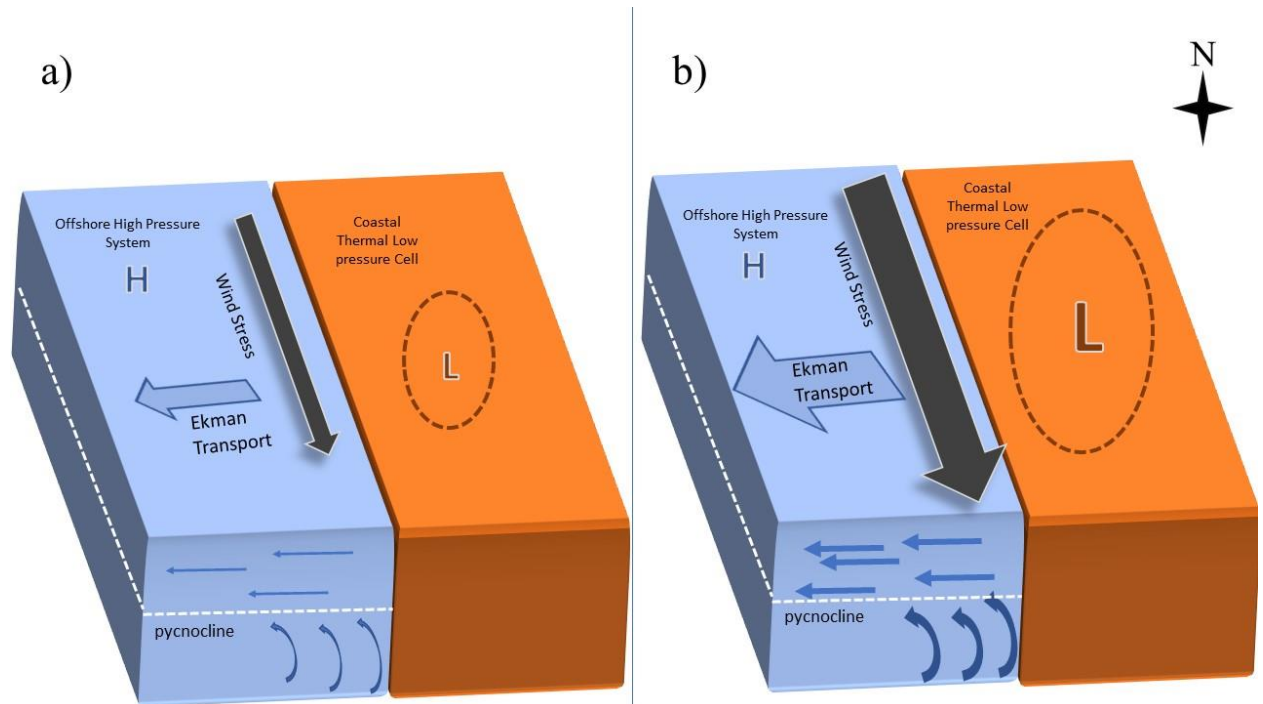
Figure 2: The Bakun Hypothesis
The present (a) and future (b) conditions of upwelling under the Bakun Hypothesis are shown above. In the future, greater heating on land than over water will increase the thermal pressure gradient between the low pressure land and high pressure systems offshore. This will strengthen upwelling-favorable winds blowing on the surface of the ocean, creating greater sheer stress on the ocean's surface and thus increasing upwelling intensity.

1.2.1 The Effect of Decadal Oscillations on Upwelling

Upwelling within the CCS is also affected by the interplay of long-term climate

oscillations in the North Pacific. Specifically, the interactions of the El Nino-Southern

Oscillation (ENSO), North Pacific Gyre Oscillation (NPGO) and Pacific Decadal Oscillation

(PDO) may play important roles in the long-term expression of upwelling in the CCS by altering

the interplay of the Pacific High and Aleutian Low pressure systems in the North Pacific. The

Aleutian Low is large, a semi-permanent low pressure system in the North Pacific. Powerful

periods of oscillation (Strong El Nino years and Strong La Nina years, for example) can become

the drivers of Pacific High/Aleutian Low movement through the excitement of atmospheric

Rossby Waves and could thus disturb the development of the winds that drive upwelling in the

CCS (Jacox et al., 2016). It has been shown in the past that the NPGO and the PDO are in part

driven by ENSO, and are more directly correlated to predicting upwelling conditions in the CCS (Di Lorenzo et al., 2010, 2008). The NPGO is the oceanic expression of the North Pacific Oscillation, a teleconnective pattern driven by the multi-year movement of the Aleutian Low in the wintertime (Ceballos, Di Lorenzo, Hoyos, Schneider, & Taguchi, 2009). ENSO Sea surface temperature (SST) anomalies in the central and southern pacific create an "atmospheric bridge," which create atmospheric variabilities that alter the location of the Aleutian Low (Di Lorenzo et al., 2010).

The PDO is a climate pattern associated with the SST change over the course of a 20 to 30-year time period. It has a positive (negative) phase – in which anomalously warm (cold) surface water exists along the west coast of North America. It is not a result of one physical mechanism, but rather the culmination of multiple mechanisms interplaying with one another: variability of the Aleutian Low pressure system, the ENSO, and anomalies in the Kuroshio-Oyashio Extension (The north flowing ocean current in the North West Pacific Ocean) (Schneider & Cornuelle, 2005).

Together, the PDO and the NPGO are the first and second most dominant oscillations in the North Pacific for SST and sea surface height anomalies, respectively. It has been shown that the PDO and NPGO are both associated with fluctuations in upwelling intensity, as well as the onset of the upwelling season (Chenillat, Riviére, Capet, Di Lorenzo, & Blanke, 2012; Di Lorenzo et al., 2008; Martinez, Antoine, Ortenzio, & Gentili, 2009). For this reason, it may be more difficult to observe long term trends the classic wind-driven upwelling model of EBUS in the CCS than in other systems. The long-term noise of these natural climate variations is challenging to differentiate from the signals of climate change in this system.

Jacox et al. 2015 found using a regional ocean model to evaluate the roles of long term climate variabilities played in the regulating upwelling in the CCS that although wind and heat

fluxes may persist in driving individual events, the PDO and NPGO affect the net result. They conclude that may make it hard to differentiate between climate change driven upwelling and these natural variabilities on multi-decadal scales of 30 years and less. Further, Jacox et al. 2016 found that the 2015-2016 El Nino was highly anomalous in its expression in the CCS in comparison to past events, and suggested that predictions of CCS conditions during an El Nino event based on tropical SST anomalies is limited to individual events. To better understand the effects of decadal oscillations within the CCS, more holistic measurements of events and regional metrics of their expressions are required (Jacox et al., 2016). The difficulty the PDO and NPGO present in modeling long term climate change effect on upwelling is seen in most recent and historical studies on the CCS (Sydeman et al., 2014; Wang et al., 2015).

1.3 The Effect of Climate Change on Sea Surface Temperature

GHGs are the most significant observed drivers of global warming over the past century (IPCC, 2014). They affect climate through radiative forcing, the measure in net change of energy caused by the introduction of GHGs. GHGs concentrate in the atmosphere and reflect energy in all directions, some of which is directed at the earth, insolating heat in our atmosphere. Radiative forcing combined with the climate's sensitivity to the forcing, results in change in temperature. Radiative forcing since 1750 has increased by over 3 W/m^2. Since 1880, the combined globally averaged and land and ocean temperature has increased by 0.85°C, while the western United States has heated by 1°-1.25°C, most of which has occurred in the last 50 years when GHGs levels have accumulated. Temperatures are expected to continue to rise considerably more depending on the GHG emissions levels (IPCC, 2014). These changes are hypothesized to impact the ecosystems of the Pacific Ocean along the west coast of North America.

1.4 Potential Impacts on Fisheries and Ecosystems

Changes in either upwelling or temperature both have the potential to impact species density, location and diversity in the coastal ocean. However, the impacts felt in coastal ecosystems would not only be seen in the trophic dynamics but would also be seen in economics of the coastal societies that use these waters. In California, Oregon and Washington (also known as the Pacific Region, as defined by the United States National Marine Fisheries Service), the economic impacts resulting from a decrease in high trophic productivity could have severe impacts on the economy. The Pacific Region is the 4th largest fishery in the United States. In 2014, 227,000 full and part-time jobs were related to the seafood industry. The total landings revenue for the region was $754 million dollars, 8% of the total US landings revenue. The level of employment in commercial fishing in the Pacific Region is as high as 12 times the average level of employment nationwide (National Marine Fisheries Service, 2014).

It is well known that fisheries rely on healthy ecosystems in order to have plentiful landings. For example, recent fishery production, which varies with SST, has significantly shrunk, from 1 million metric tons in 2006 to 97,000 tons in 2016 which may, in part, be attributable to warming ocean temperatures in the region (National Marine Fisheries Service, 2014). In 2016, the Pacific Region had to close the Pacific sardine fishery, a major staple in the region's landings. This is just one example how ecological changes can occur in the US fishing economy (National Marine Fisheries Service, 2014).

1.4.1 Potential Impacts Due to Upwelling

The impacts that could result from increased upwelling are not fully understood. One may think that an increase in upwelling activity would inherently lead to an increase in productivity through all trophic levels. However, there is also the potential for adverse consequences to organisms low on the trophic chain.

Cury and Roy (1989) hypothesize that the "Optimal Environmental Window" of upwelling intensity on the productivity of an ecosystem acts as a bell curve (Figure 3). When upwelling events are weak, productivity is limited by the scarcity of nutrients entering shallower waters where phytoplankton reside. When upwelling events are very strong, there are two potential negative outcomes. First, the deeper wind driven mixing of waters can lead to increased turbulence and therefore increased light limitation. Second, zooplankton can be pulled away
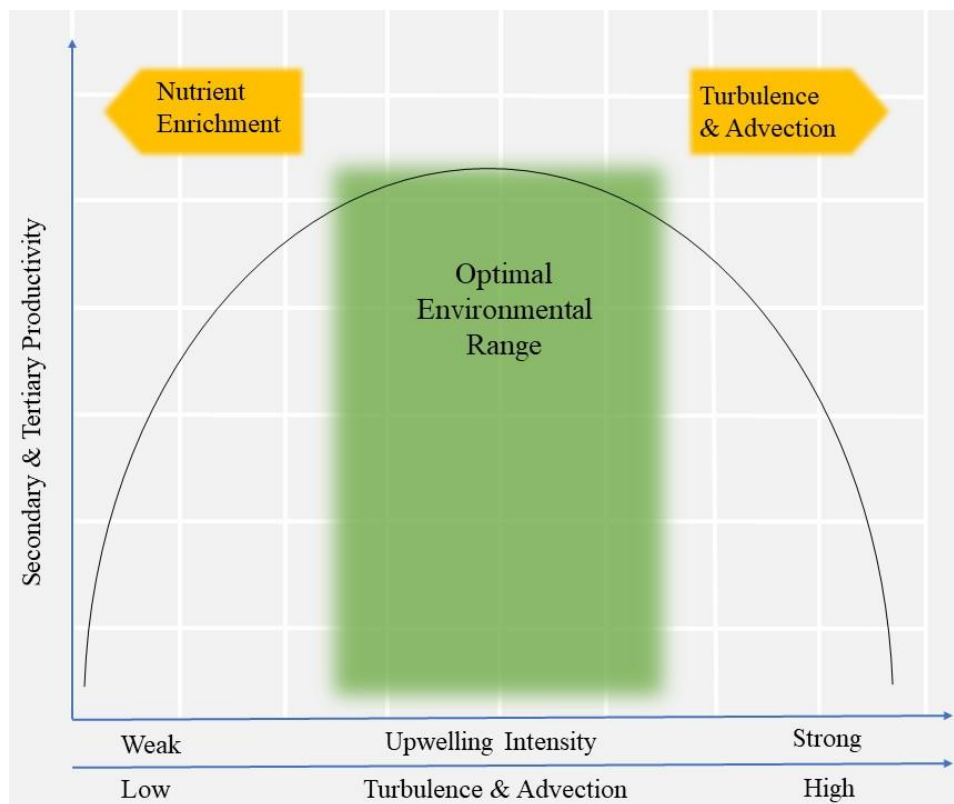
Figure 3: Optimal Environmental Window
The balance of upwelling intensity is important for EBUS ecosystems. Too little upwelling, and nutrients will not concentrate in the surface waters. Too much, and primary producers will be advected from coastal oceans, resulting in a location mismatch for primary producers and their predators (Cury and Roy, 1989).

from the shore and from the upwelling favorable areas where their phytoplankton food supply would bloom. Although there is still a potential for primary production to increase immensely, this spatial mismatch could create a missing link in the trophic chain, affecting all organisms of higher trophic levels.

Since 2002, parts of the North Pacific within the CCS have experienced seasonal summer hypoxia, growing in geographic extent and severity over time. This has been seen most infamously along the Oregon coast, where seasonal die offs of coastal organisms have become the norm. This is in part linked upwelling, which delivers nutrient-rich and oxygen-poor water into the surface layer, diluting surface oxygen levels and supporting eutrophication (Diaz & Rosenberg, 1995; Fennel & Testa, 2019; Grantham, Brian A., Chan, Francis et al., 2004; Rabalais, 2010). The potential for increased upwelling could further exacerbate hypoxia in the surface layer, causing unlivable conditions for many marine pelagic organisms.

1.4.2 Potential Impacts Due to Sea Surface Temperature

The impact of climate change on coastal SSTs may also have a role in altering the availability of food within the trophic web. Increased coastal SSTs could pose a multitude of issues. Ocean warming poses a risk to the physiological performance for numerous species issues in larval and adult stages, potentially influencing biochemical reaction rates, metabolic rates and other biological functions(Payne et al., 2016). Ocean warming could also alter a species' richness due to geographical shifts in species residence in response to a species tolerance to temperature change, which would have a direct impact to species richness and location. This could lead to cascading effects of interactions between species within an ecosystem, potentially increasing interspecies competition and species turnover (Payne et al., 2016; Pinsky et al., 2018; Wang et al., 2015).

Warmer SSTs could also cause an increase in stratification between the shallower and deeper ocean, reducing mixing potential of the ocean and therefore trapping nutrient-poor water in the shallow ocean where primary productivity almost exclusively happens. Studies have implicated stratification as one of multiple factors that can decrease in zooplankton biomass in the CCS (Payne et al., 2016; Pinsky et al., 2018). It has been suggested that increased

stratification could counteract any effects on nutrient availability observed by increased in upwelling favorable winds (Bakun et al., 2015). Increased SST could also decrease oxygen solubility in surface waters, thus further decreasing oxygen availability (Fennel & Testa, 2019).

The expectation of increased stratification, decreased oxygen solubility and decreased mixing of water would likely decrease overall ventilation of oxygen in the source waters. The interplay of increased primary productivity, increased stratification, and decreased ventilation in source waters suggest that future oceans may experience a decrease in dissolved oxygen, potentially becoming hypoxic. Indeed, there has been a long-term trend of declining oxygen content in the CCS, particularly along the Oregon Shelf, where seasonal pelagic die off has become the norm, and the Southern California Bight (the coastline from Point Conception to San Diego, known for complex ocean circulation patterns and an abundant ecosystem), where the hypoxic zone has become 80 m shallower over the period of 1984-2006 (Bograd et al., 2008; McClatchie, Goericke, Cosgrove, Auad, & Vetter, 2010). According to hydrographic observations, hypoxic events are also increasing in the northern CCS with occasional anoxic events happening around the continental shelf (Grantham, Brian A., Chan, Francis et al., 2004; Kirincich et al., 2008). These events can lead to widespread mortality of macroscopic benthic organisms and occasional dead zones.

1.5 Model Upwelling Within the California Current System

1.5.1 Recent Upwelling Models

The most recent and advanced study of Bakun's hypothesis in the CCS is "Intensification and Spatial Homogenization of Coastal Upwelling under Climate Change" (Wang et al., 2015). In their study, they test Bakun's hypothesis by analyzing historical (1950- 2005) and future (2006-2099) coastal upwelling simulations of 22 earth system models developed for the Coupled Model Intercomparison Project Phase 5 (CMIP5) along 4 major EBUS (Canary, Benguela,

Humboldt, and California). The Pacific Fisheries Environmental Lab Upwelling Index (Schwing et al., 1996) was used to define an upwelling event and derive the strength of Ekman transport during an event. Wind Stress was derived from NCEP/NCAR reanalysis data and the ERA-Interim reanalysis. Their findings indicate an increase in the amount and intensity of upwelling events, as well as a decrease in latitudinal spatial heterogeneity of the upwelling zone in all major EBUSs, except the CCS. The mechanism dictating these changes is highly positively correlated to the temperature differences between air over the ocean and coast. Specific to the CCS, they show robust correlations of weakening in amount and intensity of events, as well as spatial heterogeneity to land-ocean thermal pressure gradients. This is attributed to the unknown contributions that decadal oscillations play on the long-term observational changes to upwelling. These findings suggest that the Bakun Hypothesis may not be an accurate depiction of climate change on the CCS upwelling mechanisms.

1.5.2 The Use of Regional Climate Models Over Global Climate Models

Atmosphere Ocean Global Climate Models (AOGCMs) are the most scientifically sophisticated approach to study the complex interactions of the Earth systems in response to climate variability. The spatial grid spacing of typical AOGCM simulations ranges from around 100-250 km, which is sufficient for global and continental scale assessments of climate change but not sufficient enough to resolve the complex topography required to accurately simulate finer scale processes, such as those associated with the complex topography and coastlines of the Western US. For example, Mount Whitney and Death Valley, the highest and lowest points in the contiguous US and only around 150 km apart, are typically represented in the same model grid point with an intermediate elevation. Without the consideration of fine scale processes, the impacts of climate change at the local and regional scale must be interpreted with an added level of uncertainty (Diffenbaugh, 2005). Dynamically downscaling AOGCMs to a spatially higher

22

resolution with a Regional Climate Model (RCM) is generally considered the more robust

method used to enhance the AOGCM simulations and reduce the range of uncertainty associated

with the coarse resolution AOGCM simulations. It therefore provides a means to improve

information and reliability for climate change impacts studies. Furthermore, the large 10-member

ensemble will provide a greater measure of the uncertainty associated with intermodel

variability. This will help us minimize the impact of noise of individual models, and would thus

better support our findings overall.

For these reasons, our study will build on the findings of past studies. Wang et al. 2015,

although recent, used a coarse resolution AOGCM in their analysis. Similarly, most all past

studies have used coarse resolution models (Sydeman et al., 2014), leaving room for uncertainty

in results.

1.5.3 Scope of Project

In this thesis, we hypothesize that increasing atmospheric GHG concentrations will

significantly alter coastal ecosystems within the CCS. On one hand, increasing GHG

concentrations are hypothesized to alter mesoscale and local scale wind increasing upwelling

favorable wind conditions, and thus altering the rate of occurrence and intensity of upwelling

events. These upwelling events directly affect primary production by dictating the availability of

vital nutrients, which could have cascading effects down the trophic web. On another hand,

increasing GHG concentrations are hypothesized to increase SSTs within the CCS. These SSTs

can directly affect species density and geographic viability through heat stress, stratification and

hypoxic events.

Although Bakun's hypothesis has been extensively studied, some modeled data in the

past has been contradictory and unconfirmed (Mote & Mantua, 2002; Snyder et al., 2003).

Furthermore, recent modeling studies have all EBUSs requiring the use of coarse resolution AOGCMs (Sydeman et al., 2014; Wang et al., 2015). These models have not been able to incorporate how decadal oscillations may also affect – and potentially dominate – upwelling within the CCS over time (Jacox et al., 2015). In this thesis, a 10-member ensemble high resolution regional climate model RCM climate change experiments driven by 10 AOGCMs is used to test the aforementioned hypotheses on the CCS. A simple physically-based model is developed to measure upwelling intensity that first verified with observations and then used to evaluate potential climate change impacts on upwelling.

2 Methods

2.1 Model Simulations

Climate change experiments using AOGCM are typically performed at a spatial grid spacing of 100 to 250 km. While this resolution is sufficient for global and continental scale assessments of climate change, it is not sufficient to resolve the complex topography and coastlines required to simulate finer scale processes, such as those related to coastal responses to increased GHGs. For a conceptual example, Mount Whitney and Death Valley, the highest and lowest points in the contiguous US are often represented in the same model grid point due to their close proximity (approximately 150 km). In this case, AOGCMs provide an average climate representation of the region. Therefore, little information could be provided about the climate at these locations. As a result, RCMs are often employed to dynamically downscale AOGCM projections in a zoomed in region at a higher grid spacing (typically 15 to 50 km). Such models are used to enhance AOGCM output by using the AOGCM for lateral boundary forcing. This allows RCMs to account for both large-scale forcing at domain boundaries, as well as the effect of finer scale topography, generally allowing for a more accurate representation key climate variables such as winds and surface temperatures.

For this study, AOGCMs are used as the driving force for the Regional Climate Model system (RegCM4) at an 18-km grid spacing to form an ensemble of simulations for much of North America (Figure 4) (Ashfaq et al., 2016). Data are compiled over a 170 x 57 latitude-longitude grid of Western North America (Figure 4). This 170x57 grid will be referred to throughout out the study as the "Region of Interest" or ROI.

RegCM4 is the fourth RCM produced by the RegCM system first generated in the 1980s and features numerous updates and additions of physical parameterizations. RegCM4 is open

source, and is commonly utilized for climate change projection studies (Giorgi et al., 2012; Pal et al., 2007). Throughout this study, "ensemble" and "model average" will be used interchangeably to describe that average model values taken from this 10-member ensemble.

Table 1:A 10-Member AOGCM Ensemble Is Used as The Driver for Our Dynamically Downscaled RCM

Model	Modeling Group	Resolution (lat x lon)
ACCESS1-0	Center for Australian Weather and Climate Research, Australia	1.24 º x 1.88 º
BCC-CSM1-1	Beijing Climate Center and China Meteorological Administration, China	2.81 º x 2.81 º
CCSM4	National Center for Atmospheric Research (NCAR), United States of America	0.94 º x 1.25 º
FGOALS-g2	State Key Laboratory of Numerical Modeling for Atmospheric Sciences and Geophysical Fluid Dynamics, Institute of Atmospheric Physics, China	2.8 º x 2.8 º
GFDL-ESM2M	Geophysical Fluids Dynamics Lab, United States of America	2.0 º x 2.5 º
IPSL-CM5A-LR	Institute Pierre Simon Laplace, France	1.89 º x 3.75 º
MIROC5	Atmosphere and Ocean Research Institute (The University of Tokyo), National Institute for Environmental Studies, and Japan Agency for Marine-Earth Science and Technology, Japan	1.41 º x 1.41 º
MPI-ESM-MR	Max Planck Institute for Meteorology Germany	1.88 º x 1.88 º
MRI-CGCM3	Meteorological Research Institute, Japan	1.13 º x 1.13 º
NorESM	UNI Bjerknes Center for Climate Research, University of Bergen, Center for Intern Climate and Environmental Research, The Norwegian Meteorological	1.88 º x 2.5 º

The driving AOGCM projections are from the Coupled Model Intercomparison Project

Phase 5 (CMIP5), used in the latest Intergovernmental Panel on Climate Change (IPCC) report

(IPCC, 2014). Using the CMIP5 projections, the high-resolution RCM was driven for two 40-

year time slices: historical (1965-2005) and future (2006-2050). While 2006 is in the past, it was
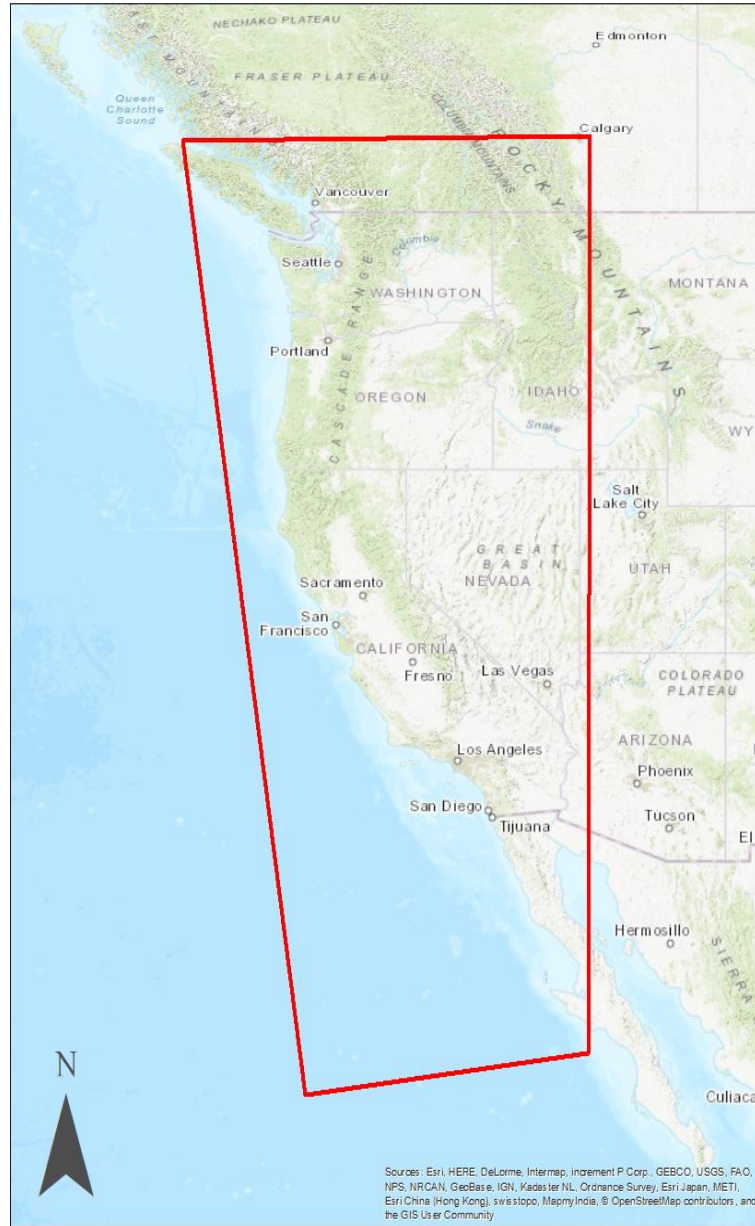
Figure 4: Area of Study
170 x 57 latitude-longitude grid of Western North America is studied in this project

considered standard by the IPCC (IPCC, 2014) to use 2005 as the starting year for the future.

Atmospheric GHG concentrations for the historical simulations are prescribed according to

observations, while the future GHG concentrations are prescribed by the IPCC Representative Concentration Pathway (RCP) 8.5. RCP 8.5 projects CO_2 concentrations to reach approximately 540ppmv by 2050. RCP 8.5 is a business as usual scenario where mankind continues to rely on fossil fuels as the dominant source of energy. RCP 8.5 GHG concentrations are considered to be relatively high, however, there is little difference between RCP 8.5 and other RCP scenario concentrations in the early and mid-21st century. For example, RCP 2.6 represents a mitigation scenario where CO_2 concentrations taper off by the end of the century; it is the least extreme of the project RCPs. CO_2 concentrations for RCP 2.6 are approximately 440 ppmv by 2050. The resulting global temperature increases of RCP 2.6 and 8.5 for 2050 are 1.75 °C and 2 °C. The less than half a degree difference at the year 2050 (even less for prior years) suggests that specific pathway is of less important for mid-century projections than for end of century projections. The RCM simulations were completed at the Oak Ridge National Laboratory's Titan, which was the world's fastest supercomputer at the time of the simulations (Ashfaq et al., 2016).

Parameters evaluated to determine any potential ecological changes include surface temperature, easterly and northerly 10-meter winds, and wind drag. All variable post-processing is completed using Python and the Environmental Systems Research Institute's Geographic Information System software (ESRI ArcGIS).

2.2 Assessing Surface Temperature

Unlike Ekman Transport and Pumping, Surface Temperature is a direct model output variable from RegCM4 at a 6-hourly interval. At each RCM grid point throughout the study area for each ensemble member, the following surface temperature statistics are computed: daily average, percent difference between the historical and future timeseries, and annual mean and maximum.

2.3 Assessing Upwelling

2.3.1 Projection Validation

The RegCM wind metrics used to calculate Upwelling are compared to observational data to validate their accuracy. The National Oceanic and Atmospheric Association Pacific Fisheries Environmental Lab's "Upwelling Index" (UI) is used as the observational data in this study (Schwing et al., 1996). The UI is based on observations of synoptic and monthly mean surface atmospheric pressure fields from the United States Navy Fleet Numerical Meteorology and Oceanography Center, and is used to validate of our model.

The UI can be calculated as follows:

$$\tau_x = \vec{v}_x |v_x| C_D$$

$$\tau_y = \vec{v}_y |v_y| C_D$$

$$\tau = \sqrt{\tau_x^2 + \tau_y^2}$$

$$\text{UI} = \frac{\tau}{f \rho_w}$$

where $\vec{v}_x$ and $\vec{v}_y$ are the northerly and easterly wind velocities, respectively and C_D is the product of atmospheric density and aerodynamical resistance, τ_x and τ_y are the northerly and easterly wind stress, respectively, f is the Coriolis force, and ρ_w is the seawater density. The UI has been used in previous studies as observational validation data. However, previous studies have used different calculations in the quantification of upwelling, rather that relying on the calculations created by the UI (Alvarez, Gomez-Gesteira, deCastro, & Dias, 2008; Pickett, 2003; Wang et al., 2015). Therefore, this study will do the same, calculating comparative UI data for validation

(described above), and data used in recent studies to quantify upwelling in CCS (described below).

2.3.2 Upwelling Calculations

To test the hypothesis that GHGs will increase upwelling favorable winds, Ekman transport and the Ekman pumping are computed based on wind stress. The sum of nearshore Ekman transport (m^3/s per 100 meters of coastline) and offshore Ekman pumping (m/s) has commonly been used to quantify coastal upwelling (Pickett, 2003; Schwing et al., 1996; Wang et al., 2015). Ekman transport $(\vec{M})$ can be calculated by the following equations:

$$\vec{M}_x = \frac{\vec{\tau}_x}{f\rho_w}$$

$$\vec{M}_y = \frac{\vec{\tau}_y}{f\rho_w}$$

where τ_x and τ_y are the northerly and easterly wind stress, respectively, f is the Coriolis force, and ρ_w is the seawater density. These equations calculate the northerly and easterly components of Ekman Transport. In order to get the correct intensity of Ekman Transport, we needed to calculate $\vec{M}$ from these components rotate $\vec{M}$ around the coastline:

$$M = \sqrt{\vec{M}_x^2 + \vec{M}_y^2}$$

$$\alpha = arctan(\vec{M}_y, \vec{M}_x)$$

$$\vec{M}_{yrot} = (\theta + \alpha)$$

$$\vec{M}_{xrot} = (\theta + \alpha)$$

$$\vec{M} = \sqrt{\vec{M}_{xrot}^2 + \vec{M}_{yrot}^2}$$

where M is the magnitude of $\vec{M}_x$ and $\vec{M}_y$, and θ is the angle of the coastline measured from east

counterclockwise (Wang et al., 2015). Ekman pumping can be calculated by the following:

$$W = \frac{\nabla \times \vec{\tau}}{f \rho_w}$$

where $\nabla \times \vec{\tau}$ is the wind stress curl and is calculated by the following:

$$\nabla \times \vec{\tau} = \left(\frac{\partial \tau_y}{\partial x} - \frac{\partial \tau_x}{\partial y} \right)$$

where $\partial \tau_y$ and $\partial \tau_x$ are the change of wind stress vector components, and ∂x and ∂y are

changes in latitudinal and longitudinal distances, respectively.

A daily moving average of Ekman transport is derived at each grid point throughout the

study area for each ensemble member based on the 6-hour values. From these daily averages, the

the seasonal start and end dates and annual mean and maximum are computed.

2.4 Analysis

2.4.1 Location Selection

A selection of nine "locations" evenly spaced along the coastline are selected assess

changes over time for certain parameters (Figure 5, Table 2). These locations were selected to

match 9 of the 15 locations used by the PFEL UI that are within the ROI. Since Ekman pumping

occurs somewhat sporadically in the open ocean (at least 25km from the coast) and there is no

observational data for comparison, we consider regional Ekman pumping as a whole, rather than

at specific locations.

Table 2: PFEL Latitude and Longitude

Latitude	Longitude
27.0	-116.0
30.0	-119.0
33.0	-119.0
36.1	-122.0
39.0	-125.0
42.1	-125.0
44.9	-125.0
48.0	-125.0
50.9	-131.0

Figure 5: PFEL Locations Used in Analysis

2.4.2 Spatial Analysis

Historical and future averages of Ekman transport, Ekman pumping, and surface temperature and differences are plotted geographically over the late spring and summer season. For this study, we define the "summer" months as May 1st - September 30th of each year. Many studies have shown that both upwelling and surface temperature are at their respective maximum magnitudes during the summer months within the CCS (Bakun et al. 2010; Bakun 1990; Wang et al. 2015; Bakun et al. 2015; Black et al. 2011; Sydeman et al. 2014). We have calculated the

geographic averages within only the summer months, in the hopes to focus in on differences occurring within the most intense times during the year.

This not only provides a visual and geographical representation of trends but also geographically locations of high intensity of changes as a result of increased GHGs. We consider the last 20 years of for each time slice: 1985-2005 for the historical period and 2030-2050 for the future projection. The difference between the two periods highlights the differences between the present day and what is projected towards the mid-century, including latitudinal trends and locations of the largest changes.

2.4.3 Time Frame Trends

Annual data provides an assessment of the trends across both time frames. A yearly mean and maximum are calculated for Ekman Transport and Ekman Pumping, while a yearly mean, maximum and minimum are calculated for Surface Temperature from daily mean data. The daily mean is calculated for Ekman Transport and Surface Temperature by taking a 5-window moving average of 6 hourly data. This results in a daily time series for each year of the two study periods (1965-2005 and 2010-2050). The yearly mean is an average of all days in the year. The yearly maximum and minimum is the maximum and minimum day in a given year, respectively. These are then used to calculate changes per decade and changes over the entire 80 year study.

2.4.4 Annual Trends

Daily mean calculations provide an assessment of the annual trends. The The daily mean is calculated for Ekman Transport and Surface Temperature by taking a 5-window moving average of 6 hourly data. This results in a daily time series for each year of the two study periods (1965-2005 and 2010-2050). The computations are averaged across at the different latitudinal locations along the coastline (Table 2, Figure 5), and averaged across all latitudinal locations.

This provides an indication of the trends at isolated locations within the CCS as well as over the system as a whole. The difference in intensity is taken between the future and historical time frames. Positive differences indicate a strengthening in intensity of the parameter, negative differences indicate a weakening in intensity of the parameter.

2.4.5 Upwelling Season Duration

We calculate the upwelling season start dates, end dates, and duration across all years in the two time frames at all coastal latitudinal locations. The upwelling season start dates and end dates were calculated from the daily averages of Ekman transport. A moving average is calculated to smooth the daily averages, and the derivative of Ekman transport intensity over time $\frac{d\vec{M}}{dt}$ is calculated.

$$\frac{d\vec{M}_n}{dt} = \frac{\vec{M}_{n-1} - \vec{M}_n}{t_{n-1} + t_n}$$

The first point of inflection of $\frac{d\vec{M}}{dt}$ is the day in which we consider the "upwelling season" to have started. The second point of inflection of $\frac{d\vec{M}}{dt}$ is the point in which we consider the "upwelling season" to have ended. The duration is defined as the number of days between the season start date and end date.

The number of upwelling events per year is an easily understood metric to help quantify the change in upwelling. We define an upwelling event as any time period greater than 24 hours that has sustained upwelling-favorable winds of greater than 12 m/s (de Miranda, Ikeda, & Rock, 1974, Cool 2019). Although the concept and definition of an upwelling event seems straightforward, calculating upwelling events has not been done in previous studies and thus would require subjective assumptions. Therefore, we use "upwelling event days" as a proxy to simplify the calculations and present more easily quantifiable findings. We calculate a daily average from 6 hourly upwelling-favorable wind stress data. We then sum the number of days that meet these criteria at each grid cell within the ROI. This results in the number of upwelling event days throughout the ROI.

2.5 Statistical Analysis

The Mann-Whitney U Test, originally developed by Mann, H.B., Whitney (n.d.), is used to compare the relatedness of historical and future values at specific RCM grid locations. The Mann-Whitney U Test is a non-parametric test on the relatedness of distributions of two independent samples. The null hypothesis (H_0) states that the two populations (X_1, X_2) have the same cumulative distribution functions (F_X), while the alternative hypothesis (H_1) states that the distributions of the two populations are significantly different:

$$H_0: F_{X1} = F_{X2}$$

$$H_1: F_{X1} \neq F_{X2}$$

For the purposes of this study, the two samples are the historical and future periods. The test is calculated according to the following:

1. Assign ranks to all observations (X_1, X_2, together), beginning with 1 for the smallest value. Equal values are handled by assigning the midpoint of unadjusted ranks.

2. Add up the ranks coming from samples 1 and 2 (R_1, R_2, respectively).

$$R_1 = \Sigma X_{R1}$$

$$R_2 = \Sigma X_{R2}$$

where X_{R1} and X_{R2} are rank values for X_1 and X_2, respectively.

3. The U statistic (U) is used for determining significance between the two sample sets and is calculated as follows:

$$U_1 = R_1 - \frac{n_1(n_1 + 1)}{2}$$

$$U_2 = R_2 - \frac{n_2(n_2 + 1)}{2}$$

where n_1 and n_2 are the sample sizes for X_1 and X_2, respectively. U can range from anywhere between 0 and $n_1 n_2$. The smaller of U_1 and U_2 is used to determine a critical value of U (U_{crit}). To determine the appropriate value of U_{crit}, the sample sizes (n_1, n_2) and the two-sided level of significance (95%, $\alpha = 0.05$ in this study) are required. If the observed value of U is less than or equal to U_{crit}, H_0 is rejected in favor of H_1 and vice versa.

The effective size (r) can be used to help describe the magnitude of the difference between the two populations X_1 and X_2 and is used to complement the significance of a U. In this case, it is the magnitude of difference between U_1 and U_2. Large datasets can magnify somewhat small changes when comparing two sample sets statistically. The effective size helps us identify when this is happening and gives us a clearer description of what the findings actually mean. Essentially, r is the fractional difference between the U statistic of the future and historical dataset, and represents the magnitude of difference, whereas p represents the

probability of the distributions happening by chance. As a dataset gets larger, p is more greatly affected by small differences in the distribution of two sets of data.

The Wendt formula is used to calculate the effective size:

$$r = 1 - \frac{2U}{n_1 \, n_2}$$

The Wendt formula is a simple rank-biserial correlation formula and has been known to have been used as an effect size measurement for the Mann-Whiteny U test (Wendt, 1968).

3 Results & Discussion

This section will cover the results of the analyses described above. It is broken up into two parts: Surface Temperature results and discussion in 3.1 and Upwelling parameters (Ekman Transport and Ekman Pumping) results and discussion in 3.2.

3.1 Surface Temperature

3.1.1 Spatial Analysis

Comparison of the two time periods shows that future surface temperature increases, most notably in the latitudes ranging from 32°-40° along the coast, ranging up 1.3° C (Figure 6). Surface temperature increases the least between 34°-40° in the open ocean (> 25km off the coast), as well as along the coast around 27°-28° off the coast of Baja California, with temperature increasing as little as 0.8°C. Therefore, all grid cells within the ROI increase in surface temperature, with increases ranging between 0.8°C-1.3°C.

Interannual variability, defined as standard deviation in this study, is seen to increase in much of the ROI, increasing most notably at 34°-40° along the coast, up to 0.15°C. The edges of the ROI (40°-50° in the North, 29°-27° in the South) show smaller levels of variability, with patches

of no variability whatsoever between the historical and future time frames. There are no areas of

decreases variability in the ROI (Figure 6).
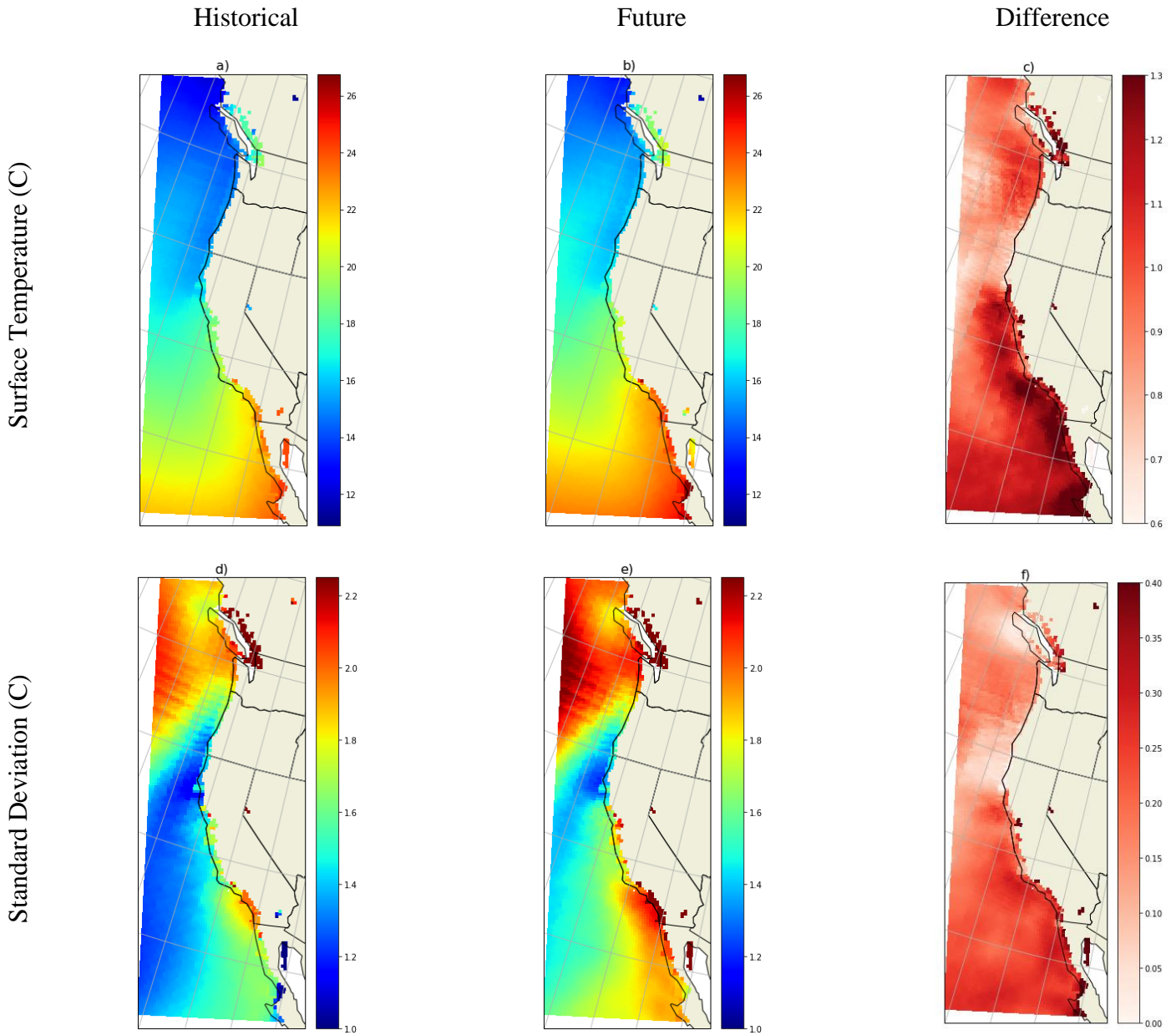
Figure 6: Surface Temperature Spatial Trends
a) and e) show the historical (1985-2005) average of surface temperature and standard deviation. b) and d) show the future (2030-2050) average of surface temperature and standard deviation. c) and f) show the difference between the future and historical edge averages and standard deviations.

An increase of 1-1.3 ⁰C is seen across the area of study, with little degree of change in the standard deviation (up to 0.15°C) across each study area
.

Our findings suggest annual trends of increasing mean, maximum and minimum intensity in

Surface Temperature across the entire region of study (Figure 7, Figure 8).
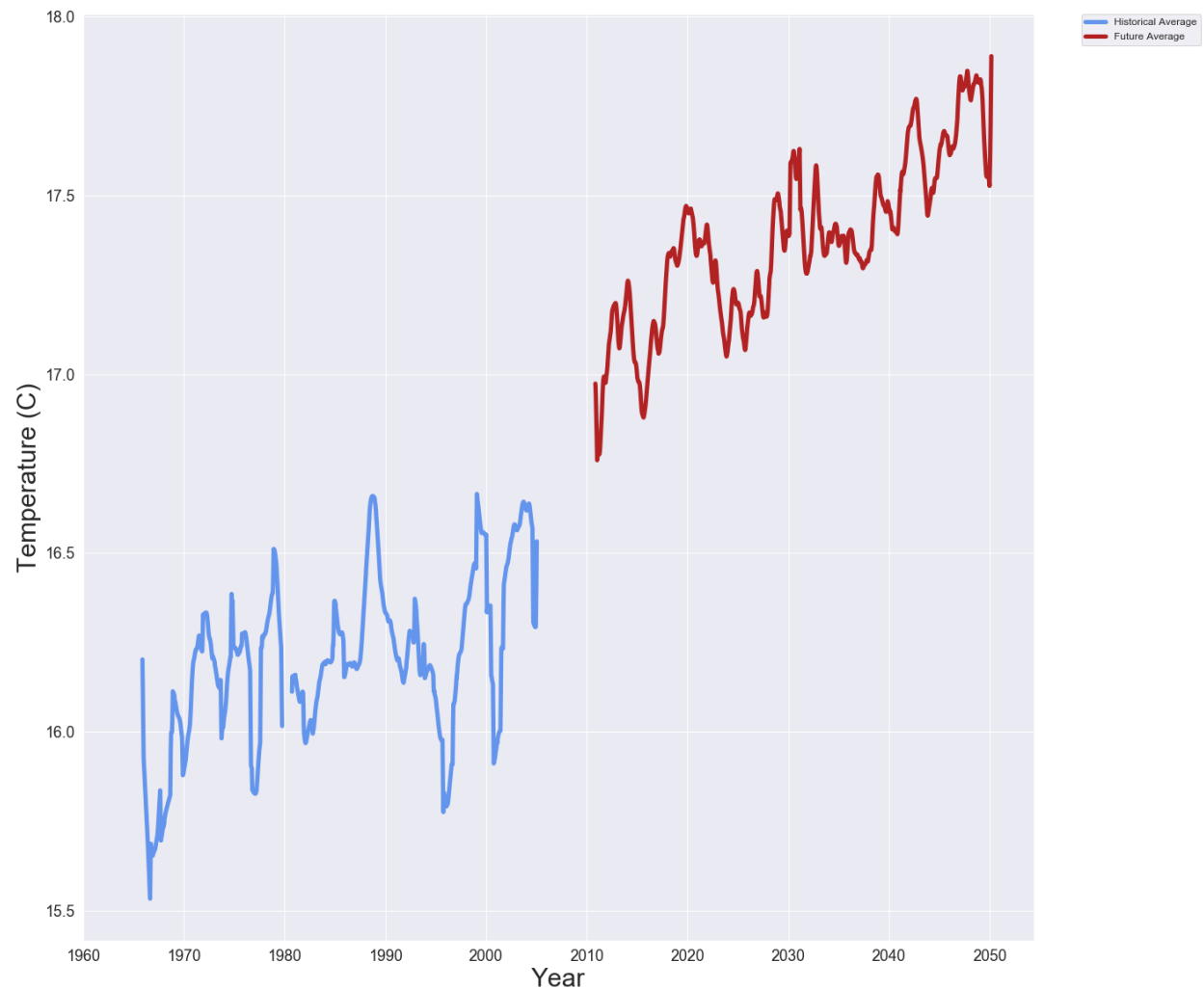
Figure 7: Surface Temperature Yearly Mean 1965-2050
The historical (blue) and future (red) projections of Surface Temperature monthly means are shown above. A increasing trend of 1-2 ⁰C is observed by 2050 in comparison to 1965.

Annual mean, maximum and minimum and trends are calculated for surface temperature

over the ROI. The annual mean increases in the future time frame (2010 -2050) when compared

to the historical time frame (1965-2005). Temperatures increase by about 0.2⁰C per decade. The

mean, maximum and minimum all show positive trends over time (Figure 8).

The average mean surface temperature increases by 0.9° C in the future time frame. A significant increase is found in the annual mean values when comparing the future time frame to the historical time frame ($p = 4.241 \times 10^{-11}$, $r = 0.83$). The average maximum annual surface temperature increases by 0.8° C, with a trend of 0.13° C increase per decade. A significant increase is found in the annual maximum values when comparing the future time frame to the historical time frame ($p = 3.535 \times 10^{-13}$, $r = 0.92$). The average minimum annual surface temperature increases by 0.7°, with a trend of 0.17° C increase per decade. A significant increase is found in the change in annual minimum surface temperature ($p = 1.814 \times 10^{-10}$, $r = 0.80$).
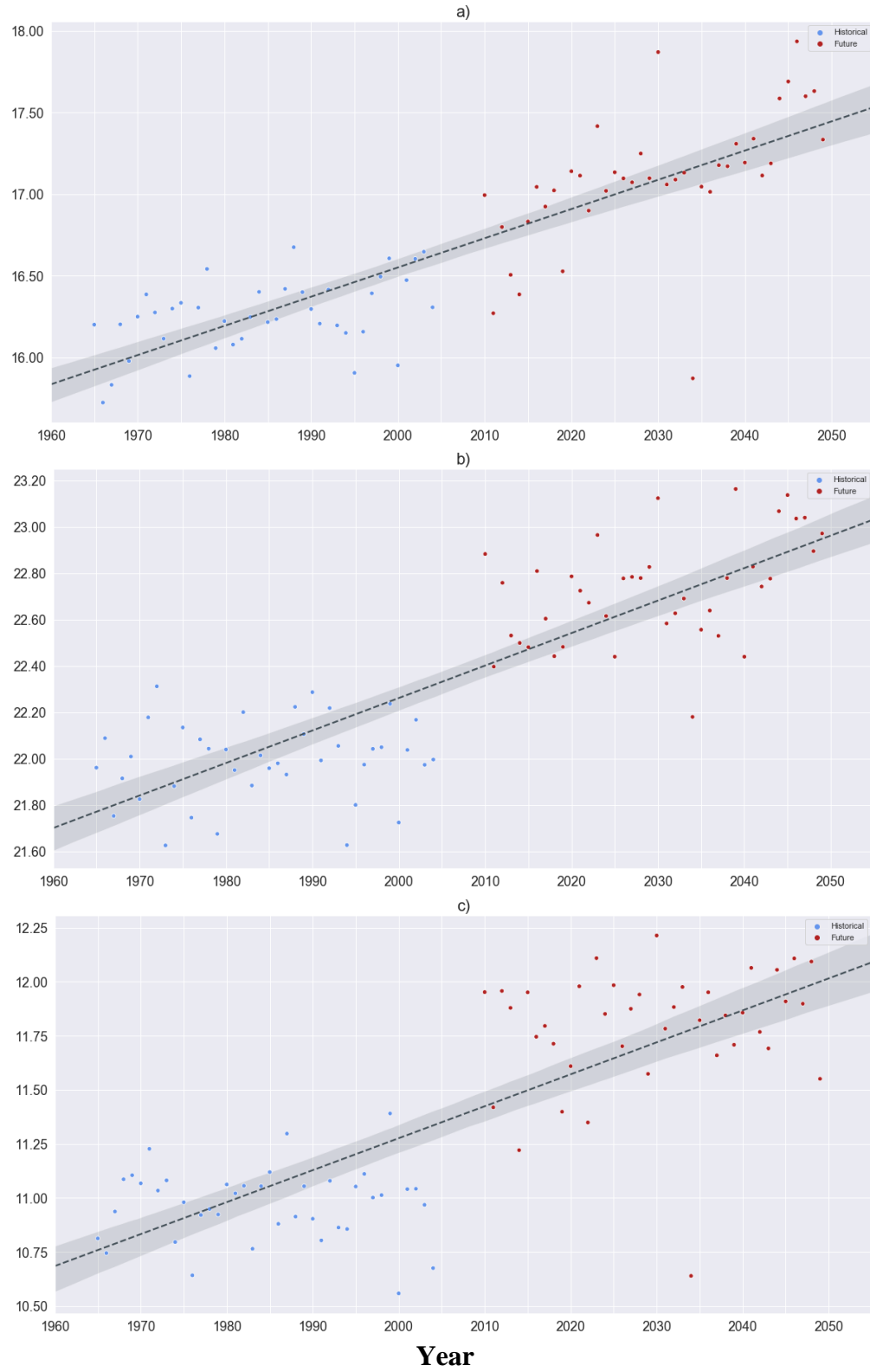
Figure 8: Surface Temperature Time Frame Statistics
Yearly mean (a), maximum (b) and minimum (c) surface temperature values for the historical (blue) and future (red) time frames, along with trend lines (dotted lines) and confidence intervals (shaded area). In all three cases, there is a trend of increasing surface temperature as time increases

In the annual mean, maximum and minimum analysis, we again see that the annual surface temperatures experience a significant increase in the future time frame (Figure 8). The annual mean, and maximum values are expected to increase in the future time frame compared to the historical time frame.

3.1.3 Annual Trends

Our findings suggest there is a robust increase in annual Surface Temperature along the coastline overall in the future timeframe of 2010-2050. Increases in Surface Temperature are robust across all locations (Figure 9, Figure 10).
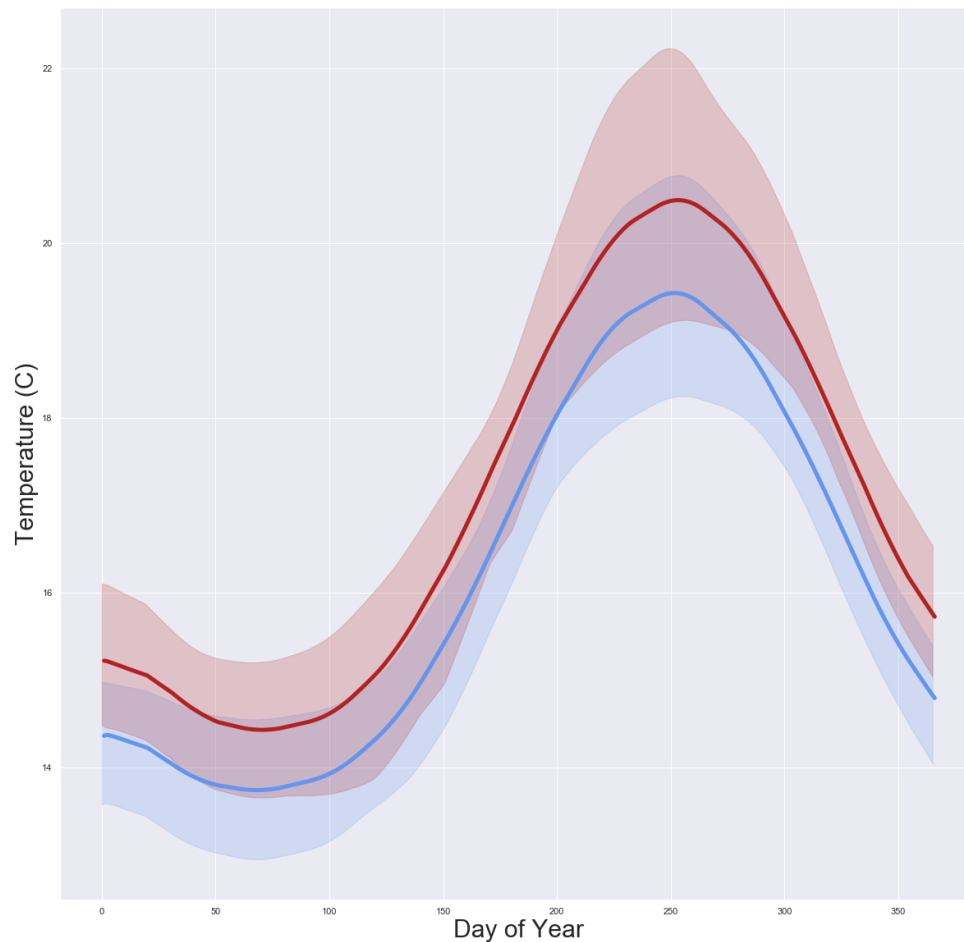
Figure 9: Surface Temperature Daily Means
Model averages of daily means of surface temperature are shown above for the historical (blue) and future(red) time frames. A historical and future average are shown as thick lines, while the shaded regions represent the ensemble minimum and maximum. The future projections are on average 1⁰C higher than the historical simulations.

There is a significant increase of 1 ⁰C in surface temperature in the future projection when compared to the historical time frame (Table 3, Figure 10). Spring shows the less temperature changes than other seasons, with March showing the smallest increases overall at 0.84⁰C (Table 3, Figure 10). The greatest increase in surface temperature happens in late summer and continues through late fall/early winter. The greatest temperature increase happens in September, at 1.17 ⁰C (Table 3, Figure 10).

Table 3: Average Surface Temperature Change by Month
Mean Surface Temperature for each month. All months show a significant increase in temperature ($p > 0.05$).

Month	Jan	Feb	Mar	Apr	May	Jun	Jul	Aug	Sept	Oct	Nov	Dec	Avg
Temperature Change (⁰C)	0.97	0.91	0.84	0.87	0.91	0.96	1.00	1.10	1.17	1.12	1.10	1.11	1.00
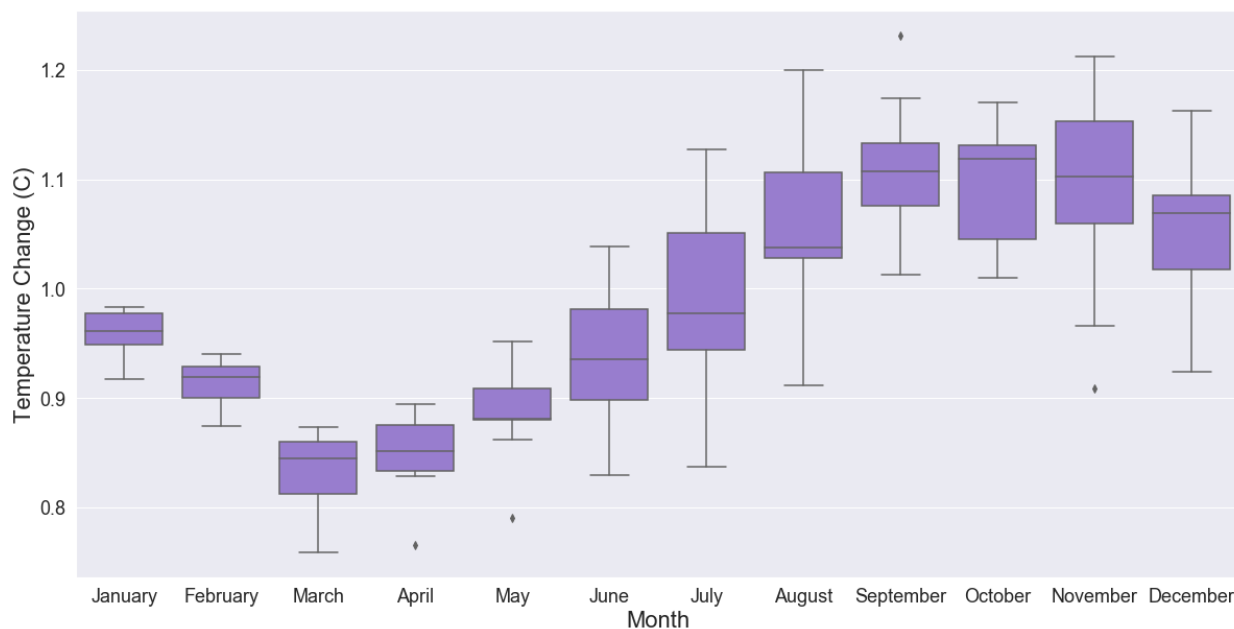
Figure 10: Average Surface Temperature Change by Month
Average surface temperature change during each month over the PFEL Comparison locations. The first, second, and third quartile are shown as a box, along with the confidence interval as whiskers. Outliers are shown as dots. Each month shows an increase of >= 0.84 ⁰C in the mean.

Each individual model shows significant increases of 0.9-1.2 ⁰C. This indicates minor variability between models and helps to further strengthen this study's findings in increasing surface temperature.

Across all analyses we see a significant increase in surface temperature. The greatest increase happens 32°- 40° along the coast, ranging up 1.3° C (Figure 6). The surface temperature annual mean increases by 0.24°C per decade (Figure), with the greatest increase coming in the months of August-November (Figure 10).

Increasing temperature could potentially have negative impacts across the food web. Increased temperatures in the ocean may also raise environmental heat stress to levels that certain species are not used to. This would directly impact species performance and could potentially cause geographical shifts in species residence. Increased temperature may also increase stratification, trapping zooplankton outside of the shallow ocean. Many fish species are dependent upon the availability of these zooplankton for survival and recruitment during larval and/or juvenile stages. Any impacts to species richness and location could have cascading effects into interactions between species within an ecosystem (Payne et al., 2016; Pinsky et al., 2018).

Increased stratification between the shallower and deeper ocean could also reduce mixing potential of the ocean and therefore trap nutrient-poor water in the shallow ocean, where primary productivity almost exclusively happens. The expectation of increased stratification and decreased mixing of water would likely decrease overall ventilation of oxygen in the source waters. With the future forecasted temperature changes, there is more potential that local oceans would have decreased concentrations of dissolved oxygen and are more likely to experience hypoxic and even anoxic events. These events can lead to widespread mortality of macroscopic benthic organisms and occasional dead zones.

Because we see robust changes at all locations across both the annual averages and summer isolation, we reject H_0, and accept H_1 that the future time frame (2010-2050) will see increases in Surface Temperature in comparison to the historical time frame (1965-2005).

3.2 Upwelling

This subsection presents results pertaining to Ekman Transport and Ekman Pumping, the two major components of upwelling. Upwelling is the event of cold, nutrient rich water being advected into surface waters, driven by surface winds. Ekman Transport occurs within the coastal ocean and is driven by wind stress, whereas Ekman Pumping occurs in the open ocean, and is driven by wind stress curl.

3.2.1 Projection Validation

To validate the accuracy of our upwelling projections, we compare our historical projections with the PFEL's UI. Daily average Ekman transport is computed for every model and averaged across locations defined in Table 2 and Figure 5. Daily averages of the UI are also calculated.

Our comparison of the historical projections to the UI (Figure 11), although having a similar bell-shape, appear to have slightly different levels of magnitude. The difference between the two data sets is statistically significant ($p=3.83\times10^{-9}$, $r=0.246$). This discrepancy in magnitude may suggest that our findings are not an accurate representation of observed intensities. As mentioned earlier, UI is derived from synoptic and monthly mean surface atmospheric pressure fields from the United States Navy Fleet Numerical Meteorology and Oceanography Center. The difference observed between the UI and our projections could be caused by the method of derivation of the index.

The difference could also be caused by the resolution of our projections. As mentioned

earlier, the resolution of our projections is 18kmx18km. A study with a much lower resolution of
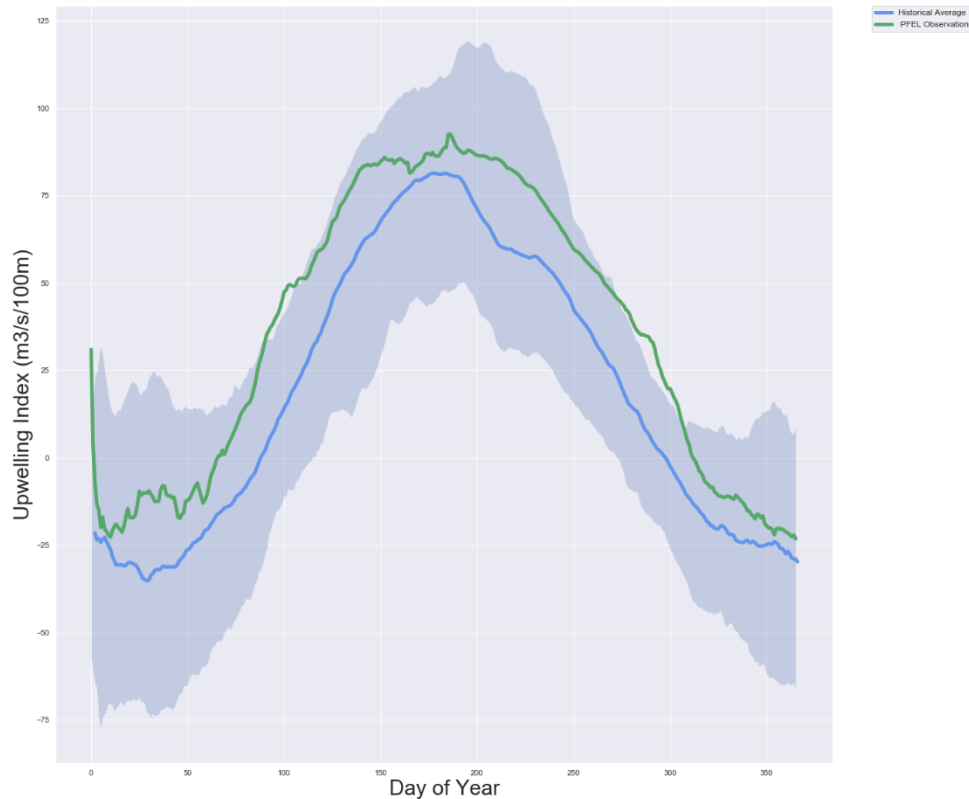
Figure 11: PFEL Comparison
Comparison of the historical projections (blue) with the PFEL UI (green). Range of historical ensemble minimum and maximum is shaded in blue. The two datasets are statistically different (< 0.05), but the bell-shaped trend gives confidence in the validity of our projections.

100km x 100km have found their predictions to accurately represent the UI observations. This

study explained that their observations, because of their resolution, captured Ekman transport

and Ekman pumping within a single grid cell (Wang et al., 2015). This study selected the single

18km x18km cell that was closest to the reported latitude and longitude location of the UI

stations. However, we may need to decrease our resolution to more accurately represent

Upwelling or create an index that measures Ekman transport and pumping as an aggregate for

comparison to the PFEL's UI.

In 2018, a study was released on the introduction of the Coastal Upwelling Transport Index (CUTI), which builds on previous indices (such as the UI used in this study) and give more accurate representation on the atmospheric and oceanic dynamics that drive upwelling in the CCS (Jacox, Edwards, Hazen, & Bograd, 2018). CUTI does this by leveraging advances in ocean and atmospheric dynamical models and be giving an updated and more complete description of coastal ocean circulations. The UI has been used historically as a validation dataset in past studies and was therefore used in this study. However, using CUTI as a comparison technique in the future may help to improve validation of our model.

Although the magnitude of the indices is different, it is important to see that the general annual trends of upwelling are similar. Both the UI's and the historical projection's annual average display a bell-shaped curve. This suggests that, although the magnitude may not be an accurate prediction of upwelling magnitude, the trends found between the historical and future time frames may still be an accurate representation of future coastal conditions.

3.2.2 Seasonal Trends

Comparison of the two time periods shows that the future upwelling is not significantly different than the historical time period (Table 4). Although the findings are not robust, there are noticeable trends in the season timing and duration. The start date of the upwelling season in the future time frame is earlier across all PFEL latitudes, with an average shift of about 16 days. The largest shifts happening between 27.0°-30.0° of about 25 days earlier. The smallest shift happens between 33.0°-39.0° of about 5-10 days earlier. The end date shifts earlier in the future as well at all PFEL latitudes except 39.0°, where the end date shifts about 3 days later. The greatest shift happens between 30.0°-33.0° of about 16-18 days earlier, and the smallest shift happens at 50.9 of about 1 day earlier. The average shift in end date is about 7 days (Table 4, Figure 12).

These shifts in season start and end dates leads to an average increase in the upwelling season duration of about 9 days, ranging as high as 19 days at some latitudes. This increase happens at all PFEL latitudes except 33.0º, where the season decreases by about 11 days, and 36.0º, where the season duration does not change (0.4 day decrease) (Table 4).

These shifts in season start dates and end dates also reveal upwelling season shifts within the CCS. From our data, we can say that although the shifts are not statistically significant, the future time frame will see an early season (earlier start date, earlier end date) than the historical season. Our historical projections show the upwelling season lasting from late May to late September. The future time frame on average shows the upwelling season starting 16 days earlier in early May, and ending 7 days earlier, in early-mid September.
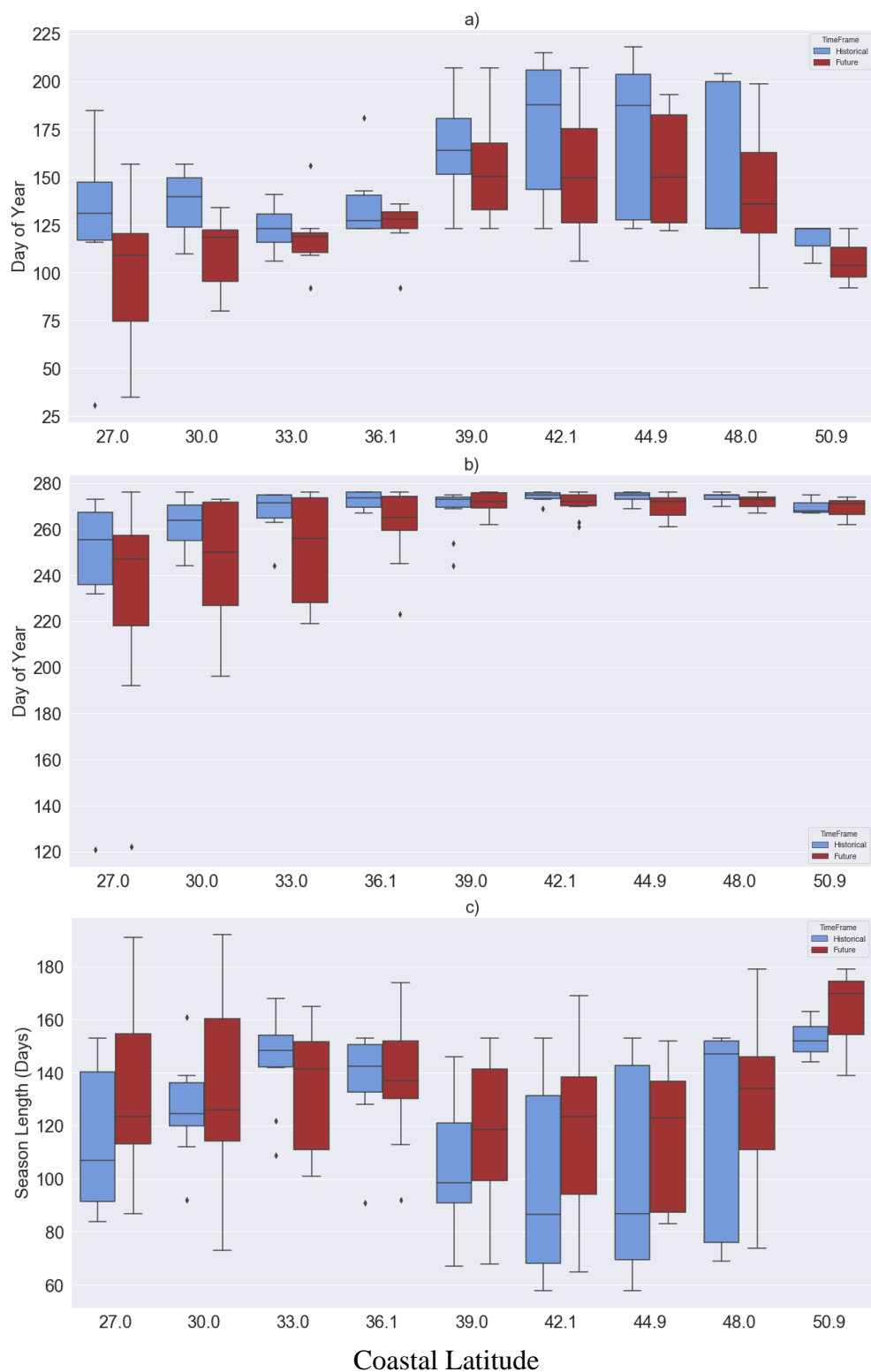
Figure 12: Season Metrics
The start data (a), end date (b) and duration (c) are shown above for future (red) and historical (blue) time frames. The first, second, and third quartile are shown as a box, along with the confidence interval as whiskers. Outliers are shown as dots Our findings suggest statistically insignificant trends of an earlier upwelling season (earlier start date, earlier end date) in the future time frame.

Table 4: Season Metrics
Start date, end date, and season duration at each PFEL location. Significant observations (p <= 0.05) are in bold.

	Start Date		End Date		Duration	
	Pvalue	**Difference**	**Pvalue**	**Difference**	**Pvalue**	**Difference**
27.0	0.13	27.3	0.63	9.9	0.226	-17.4
30.0	**0.004**	25.6	0.08	18.2	0.59	-7.4
33.0	0.42	5.0	0.06	16.2	0.24	11.2
36.1	0.15	10.4	0.06	10.8	0.96	0.4
39.0	0.41	10.1	0.46	-2.8	0.28	-12.9
42.1	0.17	22.3	0.10	3.1	0.24	-19.2
44.9	0.27	17.5	**0.041**	4.2	0.38	-13.3
48.0	0.44	13.9	0.14	1.8	0.49	-12.1
50.9	0.38	10.6	0.83	1.0	0.51	-9.7
Average	0.26	15.8	0.26	6.9	0.43	-8.9

3.2.3 Seasonal Trends: Discussion

Any changes in the timing or duration of the upwelling season can potentially alter local environments, and thus have effects on the species populations residing within that environment. The timing, duration and intensity of coastal upwelling are known to have a critical role in the phenology of key marine ecosystem processes (for example, the recruitment of rocky intertidal organisms), and changes in these upwelling characteristics have been shown to cause substantial disturbances to ecosystems at multiple trophic levels (Menge, Bruce A., Menge, 2013; Washburn et al., 2007).

As a general trend, our findings suggest the season duration increases in the future time frame, mostly due to an earlier onset of the upwelling season. This trend holds true at all latitudes, except between 36.0º-39.0º, where the season length decreases in the future (Figure

12). However, the findings are not robust (Table 4). Therefore, we accept the H_0 that there is no change in the timing or duration of the upwelling season overall.

3.2.4 Upwelling Event Days

Comparison of the two time frames shows a slight differences in the number of upwelling days per year depending on location. There are almost no locations of increasing upwelling event days, except for the lowest latitudes in the ROI (27º - 28º), which show a 1 day increase. The largest decreases happen at the upper latitudes within the ROI (45º - 50º), showing as much as a 16 day decrease. Other noticeable decreases happen between 32º - 34º and 36º - 42º along the coast, with changes ranging between 2-10 day decreases. The decreases in general are robust, whereas the increases are not robust (Figure 13).
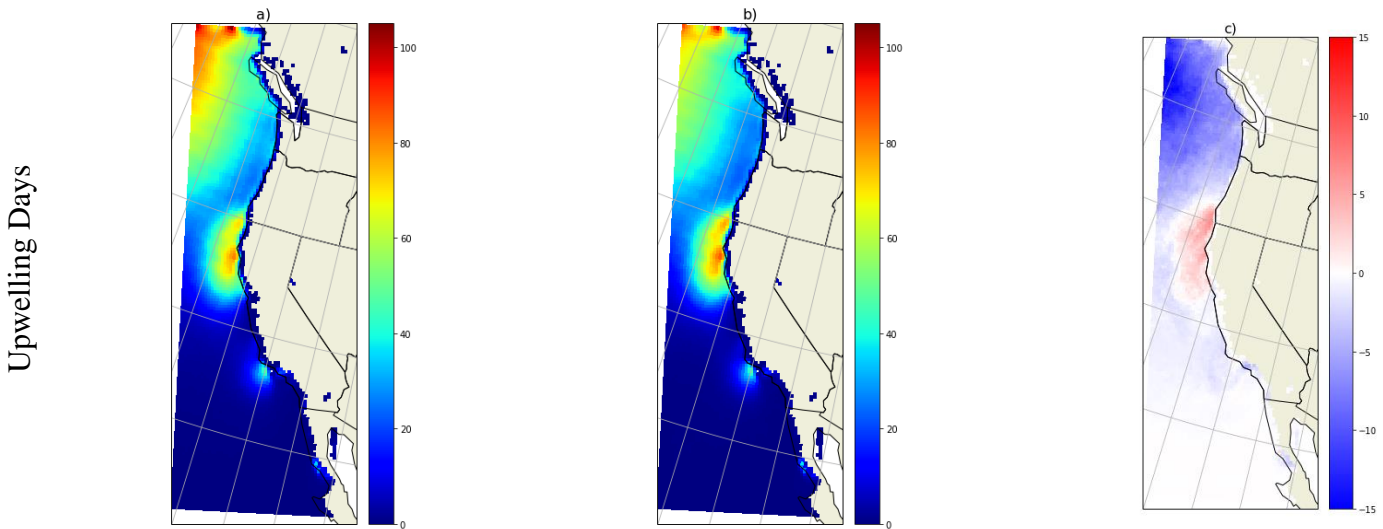
Figure 13: Upwelling Events Per Year

The upwelling events per year for the historical (a), future (b) and difference (c) are shown above. The most upwelling days per year are seen between 37º - 41º in both the historical and future time frames. In general, there is a decrease in upwelling days per year within the upper latitudes between 45º - 50º, showing as much as a 15 day decrease The largest increase in upwelling days happens between 37º - 41º of up to 5 days. The area between 27º - 28º shows no change.

3.2.5 Spatial Trends

Comparison of the two time periods shows that future Ekman Transport slightly decreases, most notably in the latitudes ranging from 34°-40° along the coast, ranging between a

2 m^3/s-6 m^3/s decrease. This range can generally be described as Point Conception to Mendocino, South to North. This upwelling range (34°-40° along the coast)of high intensity Ekman Transport is confirmed by observations in previous studies (Bakun, 1990). Ekman Transport shows little to no change at edges of the ROI (40°-50° in the North, 29°-27° in the South) (Figure 14).

Standard deviation varies throughout the ROI. The most notable decrease occurs in the range of 32⁰ – 38⁰ along the coast, decreasing as much as to 2.5 m^3/s/100m. A noticeable decrease in standard deviation is also seen between 45⁰ – 50⁰ slightly off the coast and into the open ocean. The largest increase occurs between 29⁰ – 27⁰ latitude in the open ocean displays slight increases in standard deviation, ranging around 1.5 m^3/s/100m. Other areas range between $\pm$ 1m^3/s/100m (Figure 14).

Comparison of Ekman Pumping within the ROI during the two time periods shows little to no change in general, with small blobs of varying increases and decreases in intensity. A noticeable increase in Ekman Pumping occurs in the range of 30°- 34° along the coast (within the Southern California Bight), ranging between a 1.5×10^{-5}m/s - 2×10^{-5}m/s increase. The area with the greatest decrease in Ekman Pumping occurs between 34°- 39°, ranging between a -5×10^{-6}m/s - -2×10^{-5}m/s decrease (Figure 15).

Standard deviation varies greatly throughout the ROI. The most notable decrease occurs in the range of 34⁰ – 40⁰ within the open ocean, decreasing as much as to 6×10^{-6} m/s. Decreases also occur seen between 34⁰ – 27⁰ slightly off the coast and into the open ocean. A large variation in standard deviation is seen within the range of 34⁰ – 50⁰, with only very small patches of increases and decreases (Figure 15).
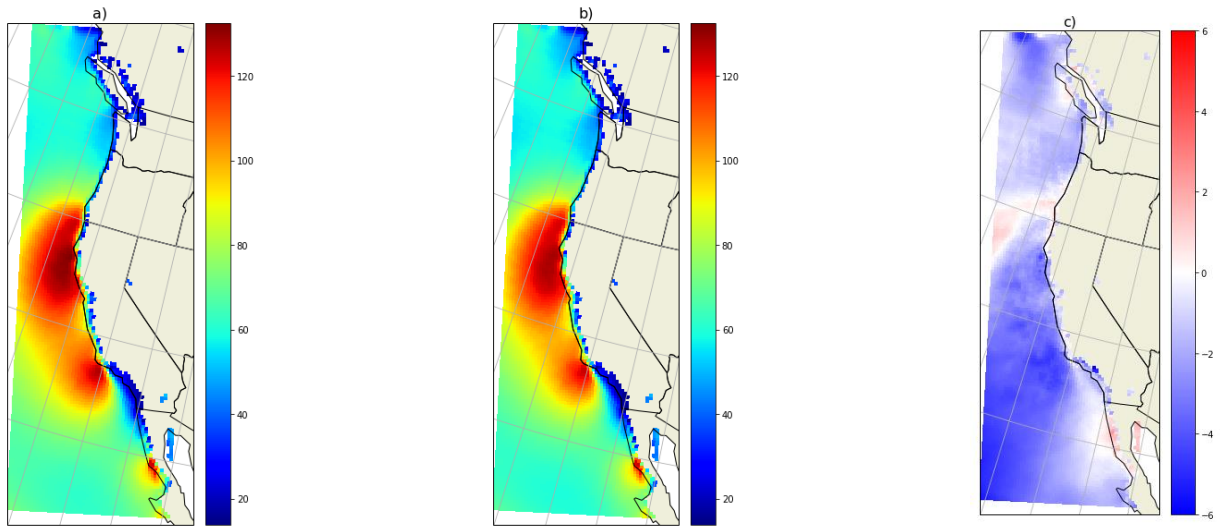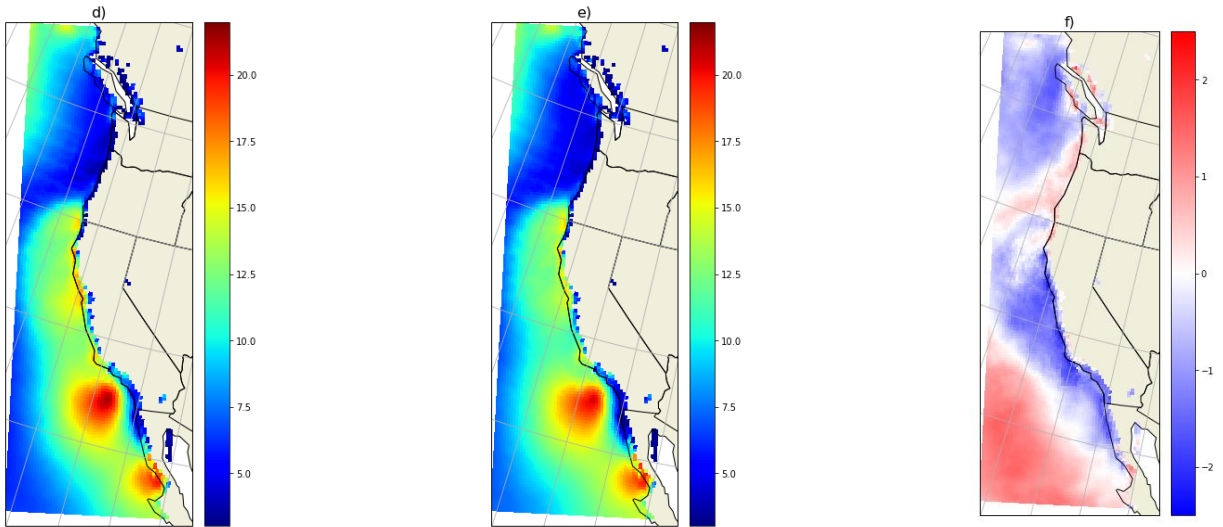
Figure 14: Ekman Transport Spatial Trends
a) and e) show the historical (1985-2005) average of Ekman transport and standard deviation. b) and d) show the future (2030-2050) average of Ekman transport and standard deviation. c) and f) shows the difference between the future and historical edge averages and standard deviations. A decrease is seen in Ekman transport around 32⁰ – 38⁰.of up to -6m3/s/100m, along with a decrease in standard deviation of up to 2 m3/s/100m
.
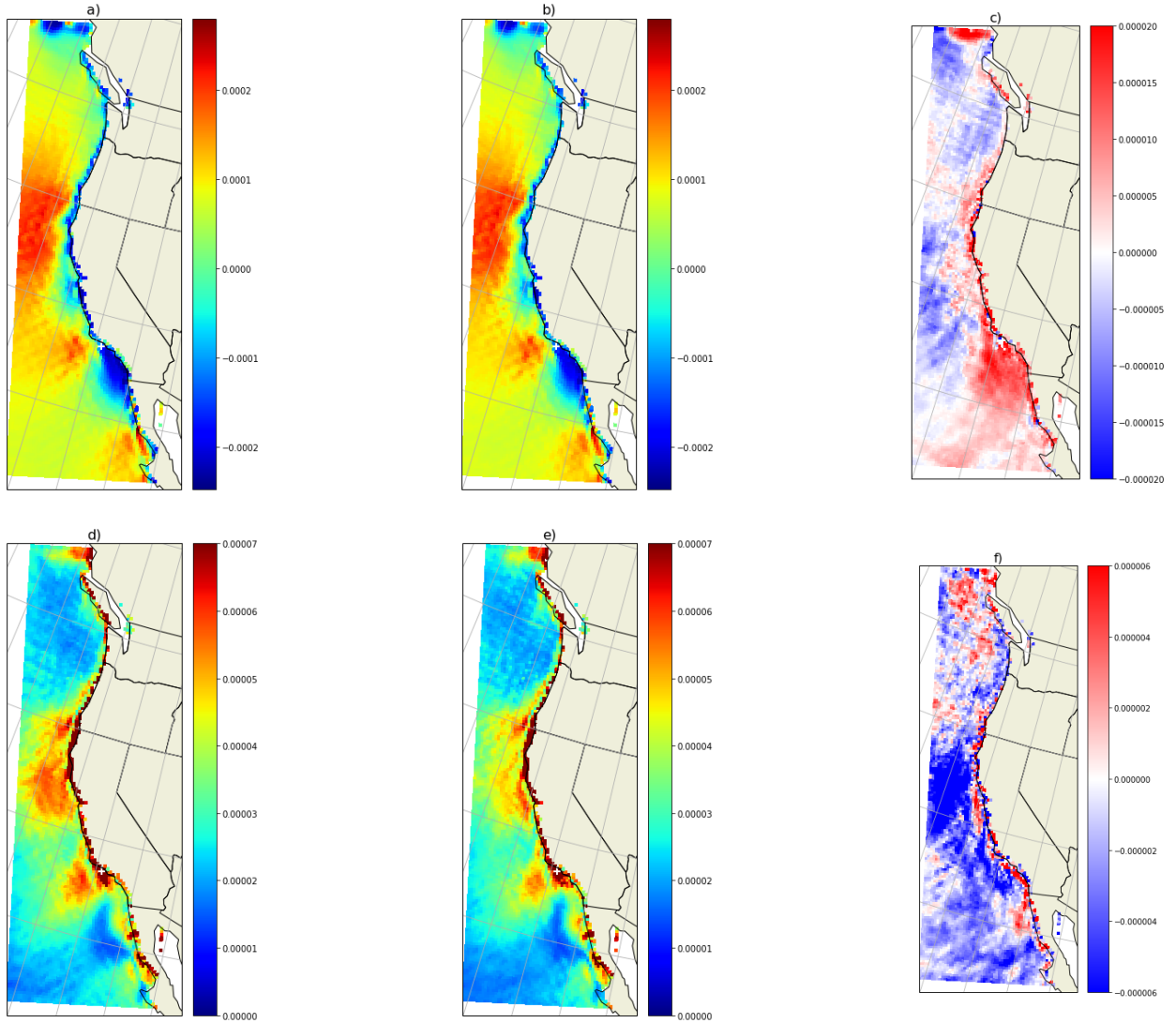
Figure 15: Ekman Pumping Spatial Trends
a) and e) show the historical (1985-2005) average of Ekman pumping and standard deviation. b) and d) show the future (2030-2050) average of Ekman pumping and standard deviation. c) and f) shows the difference between the future and historical edge averages and standard deviations. The greatest increase in Ekman pumping occurs within the Southern California bight of up to 2 x 10-5 m/s. The greatest decrease in Ekman pumping occurs in the open ocean in the range of 32º – 38º.

Our findings suggest annual trends of decreasing mean and maximum intensity in Ekman transport across the entire region of study (Figure 16, Figure 17).
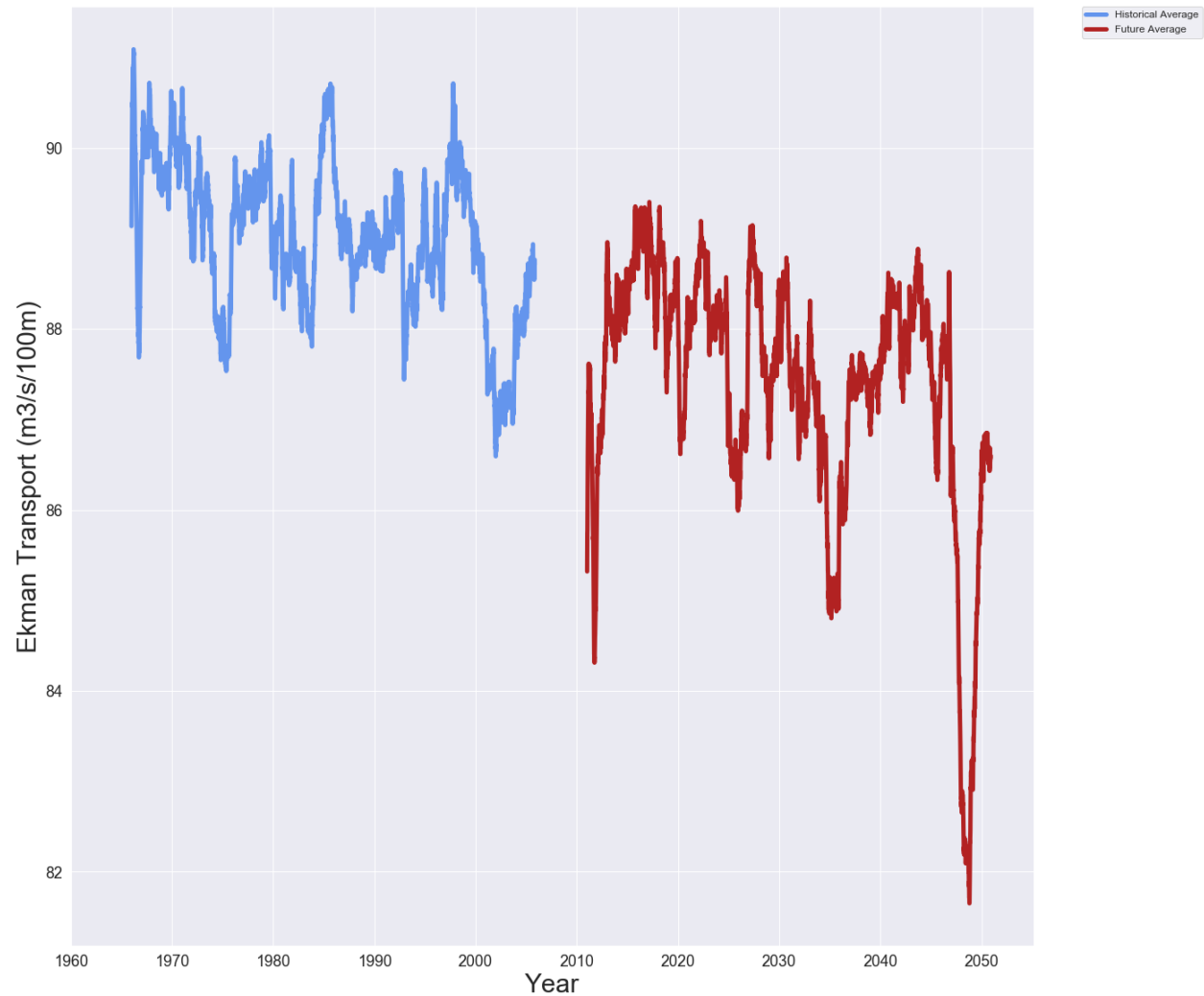
Figure 16: Ekman Transport Yearly Mean 1965-2050
The historical (blue) and future (red) projections of Ekman Transport monthly means are shown above. A decrease trend of 4-6 m³/s/100m is observed by 2050 in comparison to 1965.

The yearly mean is an average of all days in the year. The yearly maximum is the maximum day in a given year. There is a decrease in mean Ekman transport of about $6m^3$/s/100m from 1965-2050, decreasing $0.75m^3$/s/100m per decade, and a decrease in annual maximum Ekman transport of about $4.5m^3$/s/100m from 1965-2050, decreasing

0.56m³/s/100m per decade. The confidence interval appears to have a cone like shape, where the edges of the study period (1965, 2050) have the largest interval while the center of the timeframe (2005, 2010) has the smallest interval. This could potentially be explained by the lack of data points between 2005-2010, which would reduce the confidence interval during that time period. The confidence interval appears to be larger in the future time frame. However, these data are annual averages over the whole ROI, Figure displays a decrease in standard deviation between 34°-40° along the coast, where previous studies have confirmed to be the area of greatest upwelling intensity within the CCS (Bakun, 1990).

Our findings suggest slight annual trends of increasing maximum intensity in Ekman Pumping across the entire region of study, with slight decreases in the mean (Figure 18). There is a decrease in mean Ekman Pumping of about 1.1×10^{-06}m/s from 1965-2050, increasing 1.4×10^{-07}m/s per decade. There is an increase in annual maximum Ekman Pumping of about 1.1×10^{-04}m/s per decade from 1965-2050, increasing 1.3×10^{-05}m/s per decade. The confidence interval have a similar cone-like shape to Ekman Transport and Surface Temperature, and is likely caused by the same reasons. It is challenging to say if the confidence interval is larger or smaller in the future. This aligns with the findings from Figure 18, which shows extremely variable differences in standard deviation throughout the ROI.
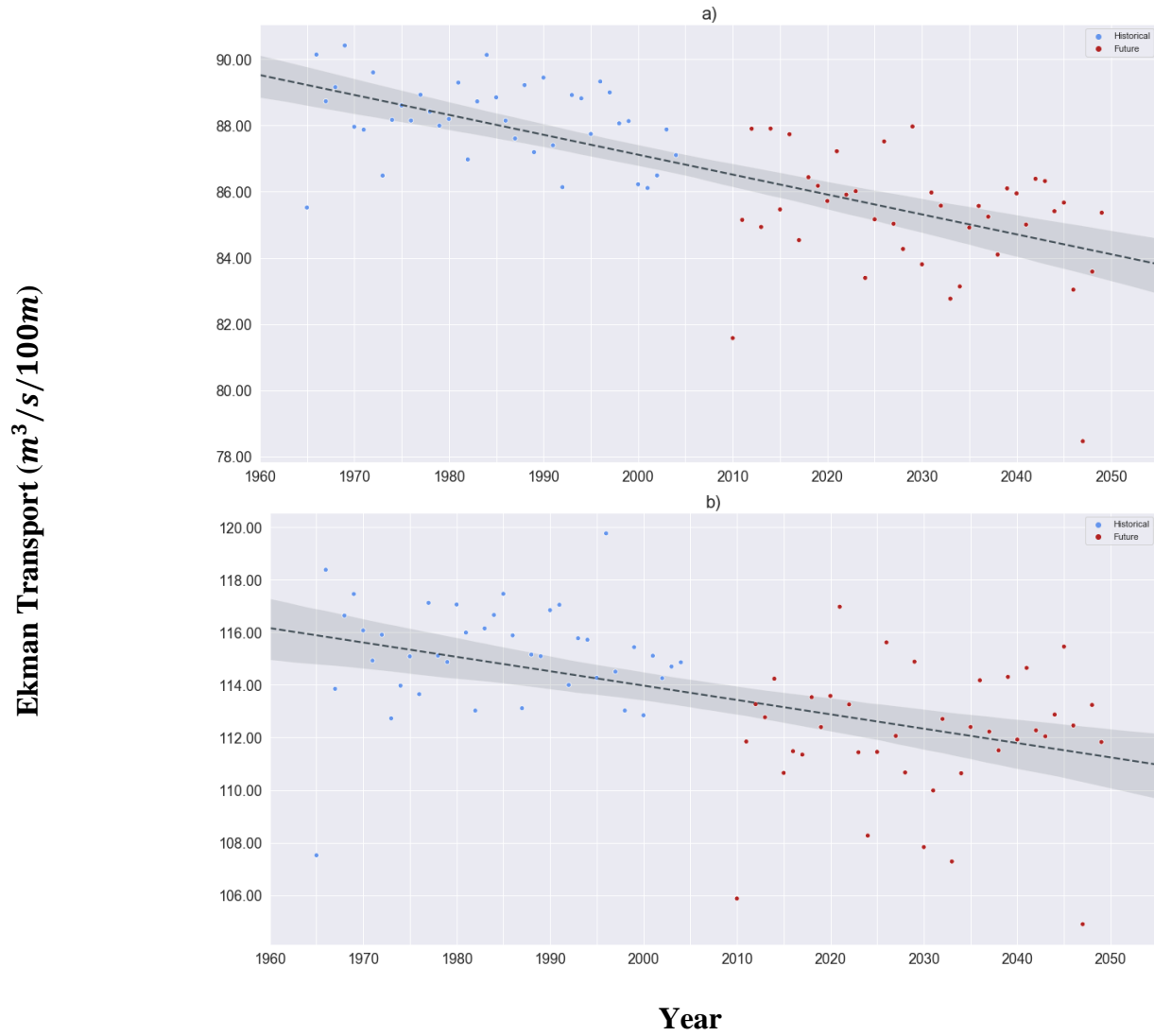
Figure 17: Ekman Transport Time Frame Statistics
Mean (a) and maximum (b) Ekman transport values are calculated for the historical and future edge time frames
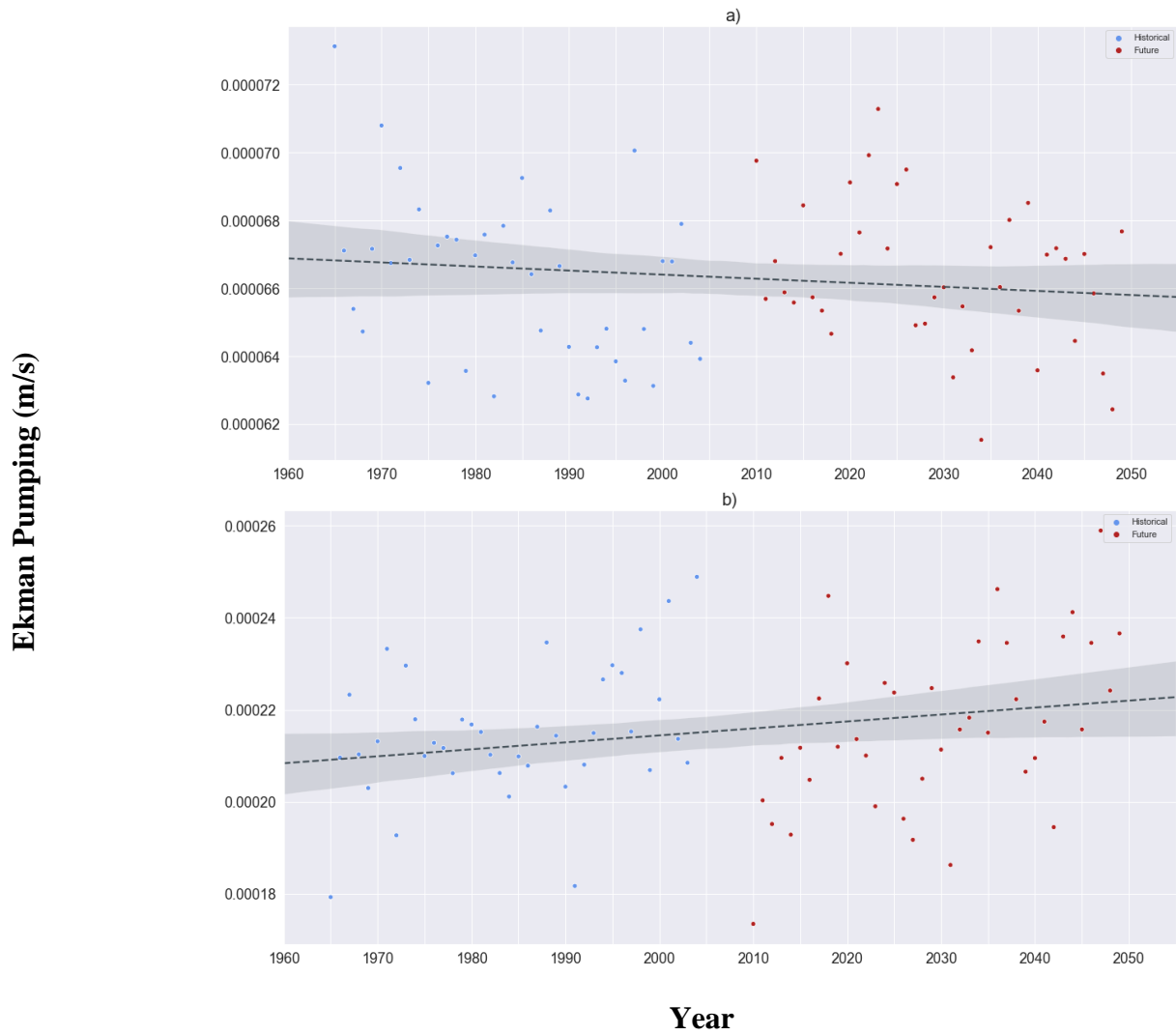
Figure 18: Ekman Pumping Time Frame Statistics
Mean (a) and maximum (b) Ekman pumping values are calculated for the historical and future edge time frames.

Our findings suggest that there are robust decreasing trends across all months in the ROI

in the future timeframe of 2010-2050 (Figure 19). There is an average decrease of 3.92

m^3/s/100m in Ekman Transport in the future projection when compared to the historical

projections (Table 5). Our findings suggest a decrease in Ekman Transport throughout the year,
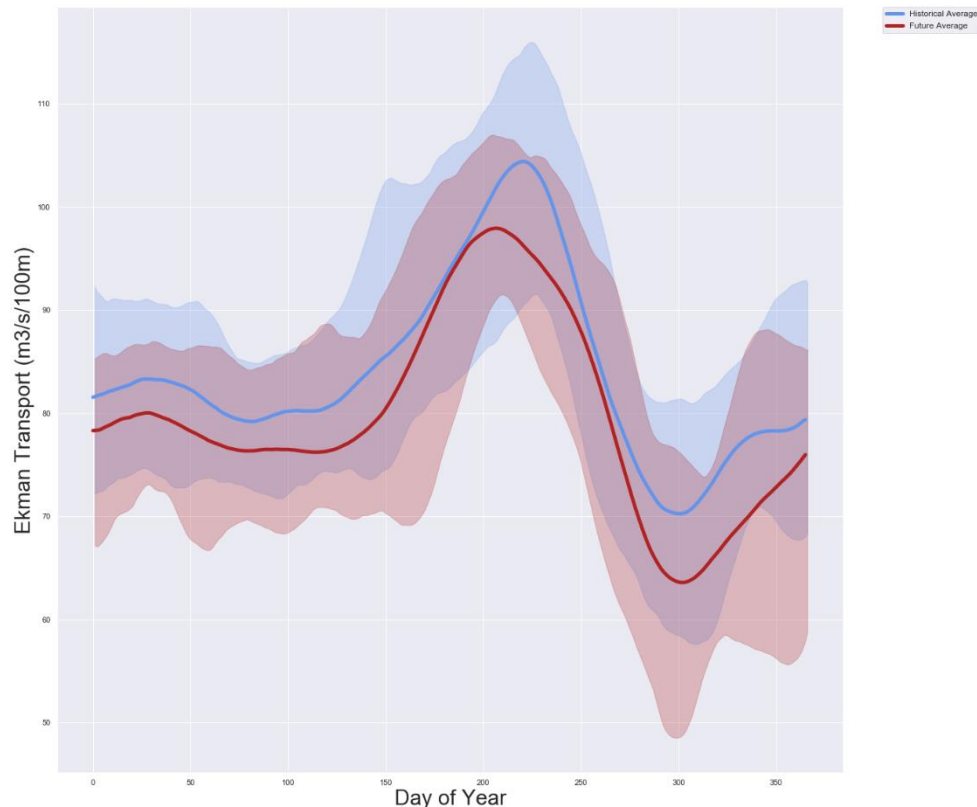
Figure 19: Ekman Transport Daily Means
Historical and Future Time Frames Model averages of daily means of Ekman Transport are shown above for the
historical (blue) and future(red) time frames. Historical and future average are shown as thick lines. Daily averages
of observations (green) were calculated from the Pacific Fisheries Environmental Lab's (PFEL) 6-hourly Upwelling
Index (UI) for the period of 1965-2005 (Schwing et al. 1996).

showing larger decreases from May – December. These decreases range from 3-5 m^3/s/100m in

general, with November showing an extreme decrease of 7.68 m^3/s/100m (Table 3). Figure 20

shows that although there is a general trend of decreases throughout the year, there is a great

amount of variability within each month.

Month	Jan	Feb	Mar	Apr	May	Jun	Jul	Aug	Sept	Oct	Nov	Dec	Avg
Ekman Transport (m³/s/100m)	-3.30	-3.84	-2.37	-2.43	-3.01	-3.08	-4.12	-4.74	-3.49	-4.95	-7.68	-3.99	-3.92

Figure 20: Average Ekman Transport Change by Month
Average Ekman transport change during each month over the PFEL Comparison locations. The same figure format is used from Figure. Each month shows a decrease of >= 2.37m³/s/100m in the mean.

3.2.8 Upwelling Intensity Discussion

Upwelling intensity is a critical component of the ecosystem. Referencing back to the "Optimal Environmental Window" (Figure 3, Cury and Roy 1989), decreased intensity can cause a decrease in nutrient enrichment and increased intensity can cause an increase in advection of phytoplankton from their food web. There is no literature specifically describing the current health of the CCS in relation to the Optimal Environmental window. However, because of the abundant ecosystems that currently exist in multiple locations along the coast in the CCS, we can assume that the system is relatively healthy (that is, within the Optimal Environmental Range described in Figure 3). If future upwelling events decrease in their intensity, the nutrient enrichment can potentially decrease. The decrease in nutrients could then potentially stifle

primary productivity performance, which could have effects throughout the trophic web of an ecosystem (Bakun et al., 2015; Bakun et al., 2010; Doney et al., 2012; Washburn et al., 2007).

A decrease in upwelling intensity would also inherently decrease the flow of cool water from depth to the surface. This cool water could serve as a buffer against the increases in radiative heat that is expected in the future (IPCC, 2014), and could thus potentially compound the stress felt by increased surface temperature.

Although Ekman transport and pumping both play a role in coastal upwelling, Ekman transport is much more powerful along the coast than Ekman pumping, and is the driver of upwelling in this region (Bakun, 1990). Decreasing trends of mean and maximum Ekman transport could therefore have a large effect on coastal upwelling intensity overall, regardless of trends seen in Ekman pumping.

The maximum upwelling intensity occurs in late June – early July (Figure 19). This aligns with previous studies, who have stated that maximum upwelling intensity is generally the summer months in the northern hemisphere (Bakun, 1990; Sydeman et al., 2014). This further adds to trends in our findings that suggest that the summer season, which ecosystems rely on for upwelling-delivered nutrients for larval survival, could be the most affected season for upwelling intensity (Figure 14)

Figure 13 shows that any decreases seen in Ekman Transport occurs along the coast between 34°- 40°, decreasing as much as to 6 $m^3/s/100m$ in the summer, an area that is known to have some of the most intense upwelling events within the CCS as well as productive coastal ecosystems (Bakun, 1990). Decreases in upwelling intensity in this region during the summer could potentially damage the productivity of a very abundant ecosystem during its most productive time of year.

The yearly maximum day of Ekman Transport intensity decreases by 0.56 m^3/s/100m per decade (Figure 17). The decrease in the maximum yearly Ekman transport could contribute to a decrease in mixing across the pycnocline, leaving the upper ocean with less nutrients essential for primary productivity and the lower ocean with a lack of oxygen.

The decreases observed in the future projections are likely linked to the decreases seen in wind stress within the region. The future timeframe will see decreases of up to 3×10^{-3} N/m^2 in the northern latitudes(44⁰-50⁰) and southern latitudes (27⁰-36⁰). The area between 36⁰-44⁰ shows slight decreases in some areas along the coast along with areas of no change (Figure 21). Wind stress is the sheer stress that sets water in motion (Figure 1) and is therefore directly linked to Ekman Transport intensity.
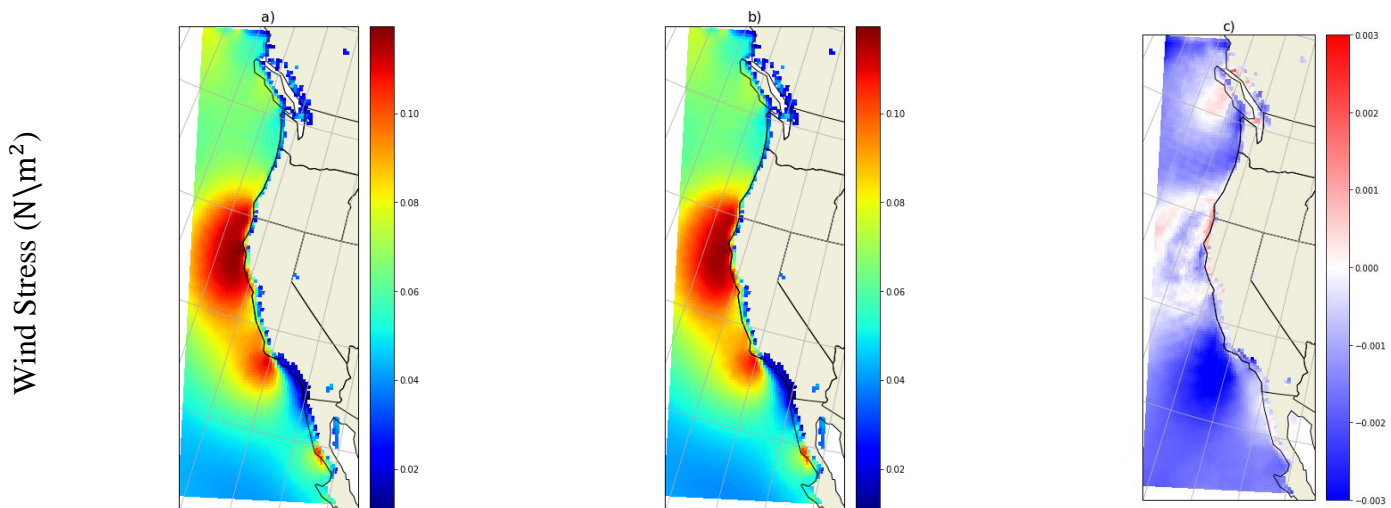
Figure 21: Wind Stress within the ROI
a) shows the historical (1965-2005) average of τ. b) shows the future (2010-2050) average of τ. c) shows the difference between the future and historical averages. Decreases are seen in general throughout the ROI of up to 3×10^{-3} N/m^2, with small sections of no change between 36⁰-44⁰.

The observed decrease in wind stress do not follow the predictions of the Bakun Hypothesis: that increasing Surface Temperatures will drive greater velocities of surface winds and therefore generate stronger wind stress on ocean surface waters, a discrepancy not seen in other major EBUSs around the world (Alvarez et al., 2008; Bakun et al., 2015; Sydeman et al.,

2014; Wang et al., 2015). This discrepancy could in part be due to the lack of understanding of effect of long term climate oscillation patterns on the CCS, and the interplay of these multiple drivers of climate variability on upwelling.

This study suggests a decrease in the number of upwelling days per year between 32⁰ - 50⁰. Upwelling days per year is a simplified version of upwelling event. It serves as a proxy to simplify the calculations and present more easily quantifiable findings. Decreases generally vary by latitude, ranging from 2-10 days between 32⁰ - 41⁰ and up to 16 days between 45⁰ - 50⁰.

This study also suggests that upwelling will significantly decrease between the ranges of 34⁰ – 40⁰ along the coast due primarily to significant decreases in Ekman Transport in the future time frame (2010-2050). Yearly Ekman Transport mean decreases 0.75 m^3/s/100m per decade, and yearly Ekman Transport maximum decreases by 0.56 m^3/s/100m per decade. The decrease is consistent in every month, with the greatest decrease happening in the middle of summer. Changes in maximum events could have important implications for ecosystems.

Ekman Pumping shows weak and inconsistent trends throughout the ROI, with decreasing trends in the annual mean and increasing trends in the annual maximum intensity. However, Ekman Transport is the dominant driver along the coastline, and Ekman Pumping trends do not appear to negate the changes seen in Ekman Transport. Because of this, we reject H_0, and accept H_1 that upwelling intensity in the Future time frame (2010-2050) will decrease compared to the Historical time frame (1965-2005). These findings suggest that Bakun's Hypothesis, which has proven to be an accurate description of increasing upwelling intensity trends within other EBUS's, may not be an accurate representation of what to expect in the California Current System as increased greenhouse gases concentrate in our atmosphere (Bakun et al., 2015; Bakun, 1990; Bakun et al., 2010; Sydeman et al., 2014). This finding is

further validated by previous studies, which find weak correlations of decreases in Future

upwelling conditions in the California Current System (Wang et al., 2015).

4 Conclusion

Our findings show a robust increase in Surface Temperature in the future. Increases in

temperature across all open ocean within the study area are expected, with increases ranging

generally from 0.8°C-1.3°C . These findings are generally accepted as accurate representations

of temperature increase under RPC 8.5/ (IPCC, 2014). Populations may be damaged climate

outside their heat tolerance capabilities, both potentially can cause physiological performance

issues as well as dictating locations viable for a species. The edge year analysis suggests that

these Surface Temperature trends are expected to magnify in their intensity as time goes on.

Our findings also show a robust decrease in upwelling intensity in the California Current

System in the future as increasing amounts of greenhouse gasses concentrate in our atmosphere.

Ekman Transport is expected to decrease by as much as 6 m^3/s/100m while Ekman Pumping is

expected to decrease by 1.1×10^{-06}m/s in the yearly average while increasing in the yearly

maximum upward velocity. The discrepancy of changing intensities in modes of upwelling could

counteract each other. However, Ekman transport is the more dominant mode of upwelling in

coastal environments.

These decreases will be most severe in the latitudes of 34°- 40° along the coastline.

Upwelling has historically been strongest within the range of 33°-39° latitude in the California

Current System (Bakun 1990), and the local environments within this range rely on the nutrients

provided by upwelling for larval survival and development. A decrease in these nutrients could

have detrimental effects on local ecosystems, starting with primary producers, and cascading up

the trophic web. Our analysis of the edge years suggests that these trends are expected to magnify in their intensity as time goes on.

Most potentially damaging from our findings is the compounding effects of warmed, oxygen diluted, stratified ocean with decreasing upwelling intensity. Upwelling, by its nature, brings cool, nutrient rich water to the surface. This phenomenon supplies coastal and open ocean ecosystems with the nutrients required for primary production, and benthic ecosystems with dissolved oxygen necessary to support species. In this sense, it acts as a buffer against stratification and hypoxia. Our findings suggest a robust decrease in this buffer, while at the same time, increasing the intensity of a major cause of stratification. This would create a compounding effect: decreased upwelling would decrease ocean mixing at thermoclines, while increased surface temperature would increase the ability of the ocean to stratify at these thermoclines. This could inhibit the advection of important nutrients into the shallow ocean and inhibit the circulation of dissolved oxygen into the deeper benthic layers.

Our findings suggest a latitudinal overlap of the locations of the most susceptible areas to these environmental factors, 34°-40° along the coastline (Figure 6, Figure 14). These environmental factors could be most severe in the summer, when there are temperature extremes and a significant decrease in upwelling intensity. These areas experience some of the strongest upwelling events within the CCS, and benefit from them by sustaining some of the most productive communities in the CCS. Our findings predict that surface and benthic ecosystems in these areas could be vulnerable as greenhouse gases continue to concentrate in the atmosphere. In the shallow ocean, decreased upwelling intensity and increased stratification will inhibit the movement of nutrients that primary producers rely on, thus stifling phytoplankton and zooplankton growth. Increases in surface temperature could also create new avenues of

environmental stress that local communities are not prepared to adapt to, resulting in decreased physiological performance and potentially geographical shifts in species residence. These changes to shallow ocean communities could have cascading effects on the availability of prey up the trophic web. In the deeper ocean, decreased upwelling intensity and increased stratification will inhibit ocean mixing, and thus decrease availability of dissolved oxygen in the deeper ocean. This could result in hypoxic and anoxic events and create major species die-off in local communities.

5 Future Recommendations

Future studies should be conducted to look to further examine the discrepancies between the PFEL's Upwelling Index and this study's upwelling intensity projections. Many past studies have used the Upwelling Index as a comparative metric to their findings, so understanding the origin of the discrepancy is important in validating the findings of this study. Exploring the use of CUTI as a validation dataset may also be worthwhile in understanding the differences between our model and comparative indices.

Future studies should also look at the importance of long-term climate oscillation patterns in the North Pacific. Some of these patterns would include the El Nino Southern Oscillation (ENSO), the Pacific Decadal Oscialltion (PDO) and the North Pacific Gyre Oscillation (NPGO), all discussed above. Passed studies have attributed comparatively weak upwelling signals in the CCS to other EBUS to the potential effects of these long term climate patterns (Jacox et al., 2015; Wang et al., 2015). Although indices for measuring the magnitude of these oscillations exist, this study used numerical projection metrics, and therefore was unable to use them for attributable analyses. Understanding the impact these oscillations is integral to getting a complete picture of future upwelling predictions in the CCS.

6 References

Alvarez, I., Gomez-Gesteira, M., deCastro, M., & Dias, J. M. (2008). Spatiotemporal evolution of upwelling regime along the western coast of the Iberian Peninsula. *Journal of Geophysical Research: Oceans*, *113*(7), 11–12. https://doi.org/10.1029/2008JC004744

Ashfaq, M., Rastogi, D., Rui, M., Kao, S.-C., Gangrade, S., Nax, B. S., & Touma, D. (2016). High-resolution ensemble projections of near-term regional climate over the continental United States. *Journal of Geophysical Research*, (3), 6578–6595. https://doi.org/10.1002/2014JD021488.Received

Bakun, A., Black, B. A., Bograd, S. J., García-Reyes, M., Miller, A. J., Rykaczewski, R. R., & Sydeman, W. J. (2015). Anticipated Effects of Climate Change on Coastal Upwelling Ecosystems. *Current Climate Change Reports*, *1*(2), 85–93. https://doi.org/10.1007/s40641-015-0008-4

Bakun, Andrew. (1990). Global Climate Change and Intensification of Coastal Ocean Upwelling. In *New Series* (Vol. 247). Retrieved from http://www.jstor.org/about/terms.html.

Bakun, Andrew, Field, D. B., Redondo-Rodriguez, A., & Weeks, S. J. (2010). Greenhouse gas, upwelling-favorable winds, and the future of coastal ocean upwelling ecosystems. *Global Change Biology*, *16*(4), 1213–1228. https://doi.org/10.1111/j.1365-2486.2009.02094.x

Black, B. A., Schroeder, I. D., Sydeman, W. J., Bograd, S. J., Wells, B. K., & Schwing, F. B. (2011). Winter and summer upwelling modes and their biological importance in the California Current Ecosystem. *Global Change Biology*, *17*(8), 2536–2545. https://doi.org/10.1111/j.1365-2486.2011.02422.x

Bograd, S. J., Castro, C. G., Di Lorenzo, E., Palacios, D. M., Bailey, H., Gilly, W., & Chavez, F. P. (2008). Oxygen declines and the shoaling of the hypoxic boundary in the California Current. *Geophysical Research Letters*, *35*(12), 1–6. https://doi.org/10.1029/2008GL034185

Ceballos, L. I., Di Lorenzo, E., Hoyos, C. D., Schneider, N., & Taguchi, B. (2009). North Pacific gyre oscillation synchronizes climate fluctuations in the eastern and western boundary systems. *Journal of Climate*, *22*(19), 5163–5174. https://doi.org/10.1175/2009JCLI2848.1

Chenillat, F., Riviére, P., Capet, X., Di Lorenzo, E., & Blanke, B. (2012). North Pacific Gyre Oscillation modulates seasonal timing and ecosystem functioning in the California Current upwelling system. *Geophysical Research Letters*, *39*(1). https://doi.org/10.1029/2011GL049966

Cury, P. M., & Roy, C. (1989). Optimal Environmental Window and Pelagic Fish Recruitment Success in Upwelling Areas. *Canadian Journal of Fisheries and Aquatic Sciences*, (April). https://doi.org/10.1139/f89-086

de Miranda, L. B., Ikeda, Y., & Rock, N. J. (1974). *Observations on Stages of Upwelling in the Region of Cabo Frio (Brazil) AS Conducted by Continuous Surface Temperature and Salinity Measurements*. 33–46.

Di Lorenzo, E., Cobb, K. M., Furtado, J. C., Schneider, N., Anderson, B. T., Bracco, A., … Vimont, D. J. (2010). Central Pacific El Niño and decadal climate change in the North Pacific Ocean. *Nature Geoscience*, *3*(11), 762–765. https://doi.org/10.1038/ngeo984

Di Lorenzo, E., Schneider, N., Cobb, K. M., Franks, P. J. S., Chhak, K., Miller, A. J., … Rivière, P. (2008). North Pacific Gyre Oscillation links ocean climate and ecosystem change. *Geophysical Research Letters*, *35*(8), 2–7. https://doi.org/10.1029/2007GL032838

Diaz, R. J., & Rosenberg, R. (1995). *Marine benthic hypoxia : A review of its ecological effects and the behavioural response of benthic macrofauna MARINE BENTHIC HYPOXIA : A REVIEW OF ITS ECOLOGICAL EFFECTS AND THE BEHAVIOURAL RESPONSES OF BENTHIC MACROFAUNA*. (January).

Diffenbaugh, N. S. (2005). Response of large-scale eastern boundary current forcing in the 21st century. *Geophysical Research Letters*, *32*(19), 1–4. https://doi.org/10.1029/2005GL023905

Doney, S. C., Ruckelshaus, M., Emmett Duffy, J., Barry, J. P., Chan, F., English, C. A., … Talley, L. D. (2012). Climate Change Impacts on Marine Ecosystems. *Annual Review of Marine Science*, *4*(1), 11–37. https://doi.org/10.1146/annurev-marine-041911-111611

Fennel, K., & Testa, J. M. (2019). *Biogeochemical Controls on Coastal Hypoxia*.

Giorgi, F., Coppola, E., Solmon, F., Mariotti, L., Sylla, M. B., Bi, X., … Brankovic, C. (2012). RegCM4: Model description and preliminary tests over multiple CORDEX domains. *Climate Research*, *52*(1), 7–29. https://doi.org/10.3354/cr01018

Grantham, Brian A., Chan, Francis, F. C., * K. J. N., * D. S. F., & Barth3, J. A. (2004). Upwelling-driven nearshore hypoxia signals ecosystem and oceanographic changes. *Letters to Nature*, *429*(June), 749–754. https://doi.org/10.1038/nature02612.1.

IPCC. (2014). *CLIMATE CHANGE 2013 - quotations*. https://doi.org/10.1017/CBO9781107415324.Summary

Jacox, M. G., Bograd, S. J., Hazen, E. L., & Fiechter, J. (2015). Sensitivity of the California Current nutrient supply to wind, heat, and remote ocean forcing. *Geophysical Research Letters*, *42*(14), 5950–5957. https://doi.org/10.1002/2015GL065147

Jacox, M. G., Edwards, C. A., Hazen, E. L., & Bograd, S. J. (2018). *Coastal Upwelling Revisited : Ekman , Bakun , and Improved Upwelling Indices for the U.S. West Coast*. 1–19. https://doi.org/10.1029/2018JC014187

Jacox, M. G., Hazen, E. L., Zaba, K. D., Rudnick, D. L., Edwards, C. A., Moore, A. M., & Bograd, S. J. (2016). *Impacts of the 2015–2016 El Niño on the California Current System: Early assessment and comparison to past events*. 7072–7080. https://doi.org/10.1002/2016GL069716.Received

Kirincich, A., Peterson, W. T., Menge, B. A., Lubchenco, J., Weeks, H., Barth, J. A., & Chan, F. (2008). Emergence of Anoxia in the California Current Large Marine Ecosystem. *Science*, *319*(5865), 920–920. https://doi.org/10.1126/science.1149016

Mann, H.B., Whitney, D. R. (n.d.). *ON A TEST OF WHETHER ONe*.

Martinez, E., Antoine, D., Ortenzio, F. D., & Gentili, B. (2009). Oscillations of Oceanic Phytoplankton. *Atlantic*, *1253*(November). https://doi.org/10.1126/science.1177012

McClatchie, S., Goericke, R., Cosgrove, R., Auad, G., & Vetter, R. (2010). Oxygen in the Southern California Bight: Multidecadal trends and implications for demersal fisheries. *Geophysical Research Letters*, *37*(19), 1–5. https://doi.org/10.1029/2010GL044497

Menge, Bruce A., Menge, D. N. L. (2013). *Dynamics of coastal meta-ecosystems: the intermittent upwelling hypothesis and a test in rocky intertidal regions*. *83*(3), 283–310.

Mote, P. W., & Mantua, N. J. (2002). Coastal upwelling in a warmer future. *Geophysical Research Letters*, *29*(23), 53-1-53–54. https://doi.org/10.1029/2002gl016086

National Marine Fisheries Service. (2014). Fisheries economics of the United States, 2014. *NOAA Technical Memorandum*, (October), 175 pp. https://doi.org/10.1017/CBO9781107415324.004

Pal, J. S., Giorgi, F., Bi, X., Elguindi, N., Solmon, F., Gao, X., … Steiner, A. L. (2007). Regional climate modeling for the developing world: The ICTP RegCM3 and RegCNET. *Bulletin of the American Meteorological Society*, *88*(9), 1395–1409. https://doi.org/10.1175/BAMS-88-9-1395

Pauly, D. ;, & Christensen. (1995). Primary production required to sustain global fisheries. In *Nature* (Vol. 374).

Payne, N. L., Smith, J. A., van der Meulen, D. E., Taylor, M. D., Watanabe, Y. Y., Takahashi, A., … Suthers, I. M. (2016). Temperature dependence of fish performance in the wild: Links with species biogeography and physiological thermal tolerance. *Functional Ecology*, *30*(6), 903–912. https://doi.org/10.1111/1365-2435.12618

Pickett, M. H. (2003). Ekman transport and pumping in the California Current based on the U.S. Navy's high-resolution atmospheric model (COAMPS). *Journal of Geophysical Research*, *108*(C10), 3327. https://doi.org/10.1029/2003JC001902

Pinsky, M. L., Frölicher, T. L., Selden, R. L., Morley, J. W., Seagraves, R. J., & Latour, R. J. (2018). Projecting shifts in thermal habitat for 686 species on the North American continental shelf. *Plos One*, *13*(5), e0196127. https://doi.org/10.1371/journal.pone.0196127

Rabalais, N. N. (2010). *Dynamics and distribution of natural and human-caused hypoxia*. 585–619.

Ruzicka, J. J., Brink, K. H., Gifford, D. J., & Bahr, F. (2016). A physically coupled end-to-end model platform for coastal ecosystems: Simulating the effects of climate change and changing upwelling characteristics on the Northern California Current ecosystem. *Ecological Modelling*, *331*(April), 86–99. https://doi.org/10.1016/j.ecolmodel.2016.01.018

Schneider, N., & Cornuelle, B. D. (2005). The Forcing of the Pacific Decadal Oscillation *. *Journal of Climate*, *18*, 4355–4373.

Schwing, F. B., O'Farrel, M., Steger, J. M., & Baltz, K. (1996). Coastal Upwelling Indices, West Coast of North America, 1946-1995. *NOAA Technical Memorandum NMFS-SWFSC-231*,

671, 1–45.

Snyder, M. A., Sloan, L. C., Diffenbaugh, N. S., & Bell, J. L. (2003). Future climate change and upwelling in the California Current. *Geophysical Research Letters*, *30*(15), 1–4. https://doi.org/10.1029/2003GL017647

Sydeman, W. J., García-Reyes, M., Schoeman, D. S. Rykaczewski, R. R. . Thompson, S. A., Black, B. A., & Bograd, S. J. (2014). Climate change and wind intensification in coastal upwelling ecosystems. *Science*, *345*(6192), 77–80. https://doi.org/10.1126/science.1251635

Wang, D., Gouhier, T. C., Menge, B. A., & Ganguly, A. R. (2015). Intensification and spatial homogenization of coastal upwelling under climate change. *Nature*, *518*(7539), 390–394. https://doi.org/10.1038/nature14235

Washburn, L., Bane, J. M., McManus, M. A., Barth, J. A., Pierce, S. D., Menge, B. A., … Lubchenco, J. (2007). Delayed upwelling alters nearshore coastal ocean ecosystems in the northern California current. *Proceedings of the National Academy of Sciences*, *104*(10), 3719–3724. https://doi.org/10.1073/pnas.0700462104

Wendt, H. W. (1968). *Dealing w i t h a c o m m o n problem in social s c i e n c e : A simplified rank-biserial coefficient of correlation based o n t h e U statistic*. 2–4.

7.0 Appendixes

Appendix A: Summary of Study Parameters

Summary of Surface temperature and Ekman transport and Ekman pumping at each study location and each model.

A.1 Surface Temperature

Timeframe	Model	27.0	30.0	33.0	36.1	39.0	42.1	44.9	48.0	50.9
Historical	ACCESS	21.21	19.63	19.67	16.89	16.63	13.49	13.24	12.71	12.03
	BCC-CSM	23.76	21.25	19.35	16.26	14.23	11.83	10.71	9.00	8.72
	CCSM4	22.76	20.77	18.85	16.92	15.42	13.45	13.08	12.00	10.84
	FGOALS	22.00	19.16	17.19	16.06	14.35	14.20	12.55	11.07	10.70
	GFDL	24.48	22.13	19.78	17.86	16.05	13.55	12.25	10.30	11.33
	IPSL	23.32	21.01	19.66	16.69	15.92	12.33	12.68	11.21	10.59
	MIROC5	23.11	21.57	19.90	18.90	15.76	14.32	13.54	13.27	12.00
	MPI	24.84	21.23	18.94	14.91	13.57	12.28	10.91	9.82	8.61
	MRI	21.32	18.99	18.60	16.80	15.63	14.35	13.71	12.54	12.31
	NorESM	23.44	21.69	20.16	17.88	16.31	14.70	13.06	11.87	10.69
Future	ACCESS	22.24	20.70	20.90	18.02	17.69	14.41	14.23	13.70	13.05
	BCC-CSM	24.74	22.51	20.66	17.76	15.70	13.16	12.11	10.53	10.23
	CCSM4	23.49	21.64	19.87	18.00	16.51	14.54	14.21	13.15	12.03
	FGOALS	23.11	20.22	18.25	17.13	15.42	15.62	13.98	12.55	11.61
	GFDL	25.23	22.80	20.54	18.76	16.92	14.41	12.99	11.02	11.89
	IPSL	24.28	21.96	20.73	17.84	17.31	13.48	13.92	12.58	11.82
	MIROC5	24.06	22.73	21.16	20.37	16.85	15.38	14.57	14.33	13.12
	MPI	25.53	22.37	20.02	15.97	14.53	13.12	11.79	10.78	9.43
	MRI	21.75	19.60	19.26	17.42	16.24	14.96	14.44	13.37	13.19
	NorESM	24.11	22.43	20.99	18.75	17.20	15.53	13.72	12.61	11.47

A.2 Ekman Transport

Timeframe	Model	27.0	30.0	33.0	36.1	39.0	42.1	44.9	48.0	50.9
Future	ACCESS	72.75	60.26	41.84	48.21	89.23	41.72	68.19	63.58	77.03
	BCC-CSM	80.60	72.28	46.45	74.69	102.80	41.75	63.04	52.29	66.23
	CCSM4	81.63	68.69	33.21	68.18	88.37	36.54	67.32	62.04	66.06
	FGOALS	97.11	75.95	47.63	67.65	87.44	42.89	55.91	54.29	60.53
	GFDL	94.13	81.46	51.02	80.02	103.21	46.39	62.65	49.38	73.03
	IPSL	81.62	71.04	45.31	70.13	87.82	26.71	60.56	48.02	59.70
	MIROC5	100.69	83.86	52.63	85.74	101.87	53.28	60.49	57.87	52.61
	MPI	63.84	47.96	27.11	51.25	83.84	39.33	55.96	50.94	68.90
	MRI	74.43	58.30	41.77	71.35	91.66	50.77	67.30	64.29	78.38
	NorESM	76.36	68.12	39.05	70.17	91.92	51.07	70.12	60.34	74.67
Historical	ACCESS	72.14	59.21	40.77	48.06	85.60	41.66	66.58	60.99	74.62
	BCC-CSM	78.59	71.48	45.03	74.24	100.85	38.89	62.09	51.62	66.39
	CCSM4	82.48	69.47	32.35	67.11	89.72	36.79	67.37	60.21	64.42
	FGOALS	94.27	74.22	45.95	65.17	85.91	41.91	52.89	49.30	53.29
	GFDL	89.55	74.72	46.22	72.30	93.31	42.14	58.92	43.12	67.48
	IPSL	79.40	69.57	43.03	66.05	81.82	18.77	54.20	41.94	52.98
	MIROC5	98.33	81.03	50.48	86.66	99.29	53.90	61.62	58.51	52.07
	MPI	63.61	50.02	29.41	52.79	83.22	37.24	53.82	49.25	64.01
	MRI	73.03	56.39	39.79	71.39	91.77	48.15	65.70	61.43	76.39
	NorESM	75.78	69.17	37.18	68.88	94.98	50.08	70.27	60.39	75.63

A.3 Ekman Pumping

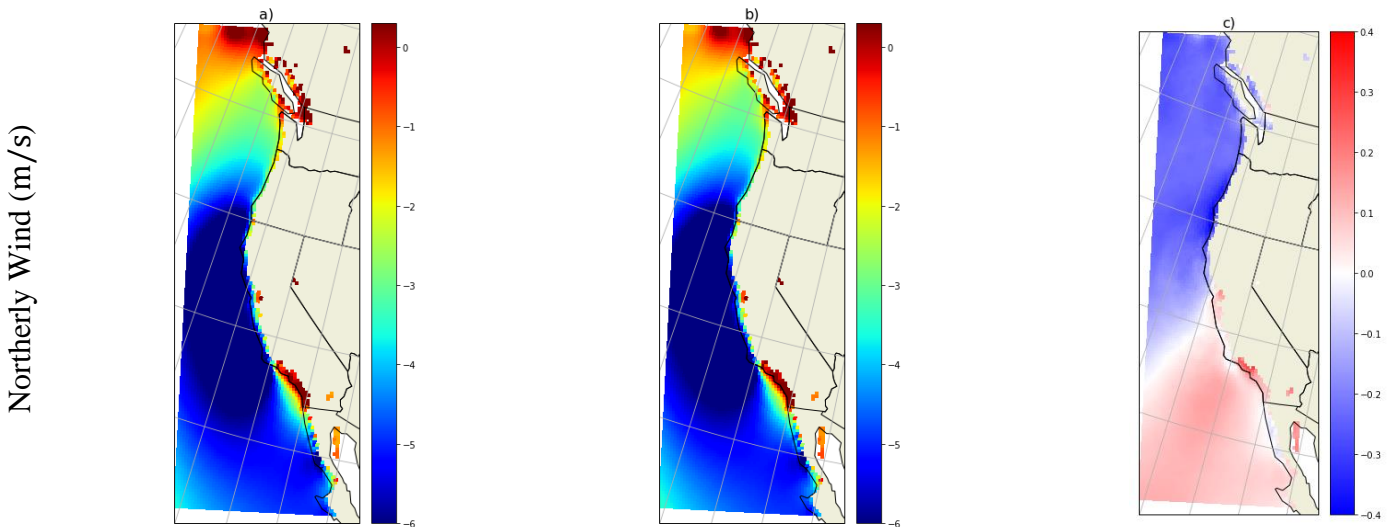| Timeframe	Model	27.0	30.0	33.0	36.1	39.0	42.1	44.9	48.0	50.9
Historical	ACCESS	-2.63E-04	4.99E-04	-1.79E-04	-2.50E-04	-2.91E-04	-3.58E-04	-1.97E-04	-1.45E-05	1.30E-04
	BCC-CSM	-1.88E-04	5.93E-04	-2.31E-04	-5.14E-04	-3.07E-04	-4.18E-04	-1.46E-04	-4.85E-06	9.99E-07
	CCSM4	-3.30E-04	6.95E-04	-1.73E-04	-3.69E-04	-2.10E-04	-3.85E-04	-2.31E-04	-4.49E-06	7.77E-05
	FGOALS	-3.22E-04	6.45E-04	-2.16E-04	-4.43E-04	-1.52E-04	-2.32E-04	-9.43E-05	1.55E-04	8.36E-05
	GFDL	-2.84E-04	6.64E-04	-2.25E-04	-4.82E-04	-2.71E-04	-3.60E-04	-1.21E-04	2.32E-05	8.52E-05
	IPSL	-2.50E-04	7.80E-04	-1.97E-04	-3.96E-04	-2.21E-04	-3.60E-04	-2.24E-04	-4.94E-05	2.83E-05
	MIROC5	-4.24E-04	6.51E-04	-2.94E-04	-5.07E-04	-4.15E-04	-5.94E-04	-2.28E-04	3.82E-07	2.75E-05
	MPI	-1.78E-04	2.95E-04	-1.06E-04	-3.32E-04	-1.73E-04	-3.61E-04	-1.14E-04	-4.64E-05	-7.81E-05
	MRI	-3.58E-04	5.79E-04	-1.69E-04	-3.51E-04	-1.28E-04	-1.05E-04	1.25E-05	7.20E-05	1.52E-05
	NorESM	-2.70E-04	6.64E-04	-1.89E-04	-4.13E-04	-3.39E-04	-7.36E-04	-4.22E-04	-7.22E-05	8.32E-05
Future	ACCESS	-2.67E-04	5.26E-04	-1.83E-04	-2.64E-04	-2.35E-04	-3.14E-04	-1.92E-04	-6.09E-06	1.40E-04
	BCC-CSM	-1.74E-04	6.36E-04	-2.40E-04	-5.10E-04	-2.90E-04	-4.39E-04	-1.68E-04	-1.62E-05	3.34E-06
	CCSM4	-3.59E-04	7.23E-04	-1.81E-04	-3.74E-04	-2.34E-04	-4.42E-04	-2.90E-04	-6.61E-06	7.19E-05
	FGOALS	-3.27E-04	6.08E-04	-2.05E-04	-4.74E-04	-1.73E-04	-2.24E-04	-8.82E-05	1.24E-04	5.50E-05
	GFDL	-2.73E-04	6.35E-04	-1.95E-04	-3.93E-04	-2.40E-04	-3.96E-04	-1.85E-04	4.84E-06	7.37E-05
	IPSL	-2.79E-04	7.72E-04	-1.83E-04	-3.50E-04	-1.70E-04	-3.14E-04	-2.66E-04	-5.50E-05	1.85E-05
	MIROC5	-4.03E-04	6.72E-04	-2.99E-04	-4.98E-04	-4.18E-04	-6.13E-04	-2.33E-04	-3.30E-06	2.88E-05
	MPI	-1.87E-04	3.36E-04	-1.16E-04	-3.28E-04	-1.60E-04	-3.66E-04	-1.31E-04	-4.90E-05	-6.96E-05
	MRI	-3.78E-04	5.99E-04	-1.56E-04	-3.58E-04	-1.36E-04	-1.19E-04	3.34E-06	6.42E-05	7.41E-06
	NorESM	-3.07E-04	6.61E-04	-1.81E-04	-4.35E-04	-3.56E-04	-7.68E-04	-4.17E-04	-7.67E-05	8.05E-05

Appendix B: Wind Metrics

Wind metrics part of the calculation of upwelling are analyzed over the study area. Below shows the summer average of historical (1985-2005) and future (2030-2050) magnitudes and standard deviation of easterly winds ($\vec{u}$), northerly winds ($\vec{v}$), and winds rotated parallel to the coastline (upwelling favorable) ($\vec{w}_{\parallel}$). a) and d) show the historical magnitude and standard deviation, respectively. b) and e) show the future magnitude and standard deviation, respectively. c) and f) show the Difference between the two timeframe's (future – historical) magnitude and standard deviation, respectively.

B. 1 $\vec{u}$

B. 2 $\vec{v}$

B.3 $\vec{w}_\parallel$

Drag Coeficient (m/s)